ISAS - INTERNATIONAL SCHOOL
FOR ADVANCED STUDIES

Some Theoretical Surprises
on a Germanium Surface

Thesis submitted for the degree of
Doctor Philosophiae

CANDIDATE: SUPERVISORS:
Gerardo Ballabio   Erio Tosatti
                              Sandro Scandolo
                              Stefano de Gironcoli

October 2001

Some Theoretical Surprises
on a Germanium Surface

Thesis submitted for the degree of
Doctor Philosophiae

CANDIDATE: SUPERVISORS:
Gerardo Ballabio   Erio Tosatti
                        Sandro Scandolo
                    Stefano de Gironcoli

October 2001

Contents

4

Introduction

An important branch of solid-state physics is the study of surfaces and interfaces, where many interesting phenomena often occur. The main feature in surface physics is reconstruction of solid surfaces, i.e., atoms near the surface rearrange themselves in a different crystal structure than that of the bulk material. This is especially true in the case of semiconductors, which form strong and directional bonds between atoms: if the bulk crystal is truncated at a given surface, a lot of dangling bonds are created, i.e., half-filled orbitals pointing outwards the surface. Since dangling bonds are energetically very unfavourable, semiconductor surfaces usually show a strong tendency to reconstruct in order to reduce their number.

In the last decades, along with the extremely fast development of powerful computers, computational methods have been acquiring an ever more important role in many fields of physics. They are especially useful in the study of solid systems, which by their nature, except for the simplest cases, are too complex for an analytical treatment. By appropriate, quantum-mechanical computational methods, many properties of solid materials can today be calculated to very high degrees of accuracy, including properties that aren't directly accessible by experimental methods, and can provide considerable insight for the comprehension of such systems.

In the main course of my Ph.D. research, I undertook a computational study of a specific system, namely, the Sn-covered Ge(111) surface. This surface has recently attracted great interest since the discovery of a puzzling temperature-driven phase transition. What has been observed is that, below a critical temperature (about −60°C), the reconstructed surface further distorts reversibly, lowering the surface symmetry: the main structural feature of the distortion is a displacement of adatoms orthogonal to the surface plane, some of them going "up" while some going "down". The physical mechanism underlying this phase transition is still highly controversial.

By numerical computation, using the *ab initio* DFT-PW (density functional theory, plane waves expansion) method, we checked and confirmed findings by other workers, and collected new evidence to help explaining the

5

behavior of this surface. While a complete understanding of the physics of the Sn/Ge(111) surface is still lacking, this work clarified several aspects of the problem. It was found that the electronic charge rearrangement accompanying the distortion is largely intraatomic, with little or no charge transfer between adatoms: hybridization between the Sn adatoms' dangling bonds, backbonds and a deeper lying second-third layer bond must thus be taken into account, making it impossible to describe the distortion within a single-band picture. In particular, the interpretation of the distortion as a charge-density wave transition, as was proposed by its discoverers, must be rejected.

A completely new aspect of this surface's behavior was found by investigating the response of the system under surface strain. Computations show that, when a compressive or expansive strain is applied, the distortion pattern *qualitatively* changes, varying the relative population of "up" and "down" adatoms by discrete amounts ranging from "all down" to "all up". The data indicate clearly that the adatom geometry, in particular their heights, can jump between two distinct local energy minima, possibly associated to different valence states. Because of the triangular nature of the adatom lattice, the surface might behave as a frustrated mixed-valence system.

Another unrelated and parallel piece of work that I did during my Ph.D. is a computational study of the high-temperature phase of the Ge(111) surface. This system shows a first-order phase transition above room temperature (at about 540 K), and while the insulating room-temperature phase is very well characterized, the structure of the high-temperature phase, known to be weakly metallic, hasn't been so intensely studied. I performed numerical computations, using the empirical tight-binding method, on a model proposed for this phase (the Phaneuf-Webb model), and compared them with experimental data. A gratifying agreement between experiment and theory was found, strongly supporting the validity of the Phaneuf-Webb model. The weak metallicity can be attributed by surface "doping" by surface defects that are intrinsic in this model. An interesting emerging concept is that these defects exhibit fractional charge, donating exactly half an electron to the surface bands.

The plan of this thesis has been arranged so as to introduce briefly in chapter 1 the computational methods used, and then subsequently to discuss in chapters 2–6 different points on the physics of our semiconductor surface, encumbered by the necessity to describe technicalities case by case. Chapter 6 contains our provisional conclusions, still relatively open at the time of this writing, on Sn/Ge(111). Chapter 7 is, as announced, devoted to the separate problem of Ge(111).

The list of the main new results obtained in the course of this thesis work

is the following:

1. We have shown (chapter 2) that the reason for enhanced stability, in the $\sqrt{3} \times \sqrt{3}R30°$ structure, of a tetravalent adatom with large atomic number, such as Sn and Pb, on Ge(111) (and presumably also on Si(111)) is the increased interaction with the second-third layer Ge-Ge bond directly beneath. This is in turn encouraged by the large adatom size, forcing a downward shift of its dangling bond energy.

2. We have analyzed (chapter 3) the energetics of the 3×3 distortion of Sn/Ge(111) and found that the gain comes from electron kinetic energy, at the expense of electron-ion, electron-electron and ion-ion energy. This points towards a strong intra-adatom dehybridization and to a modulation of the bond with the substrate as the driving mechanism, and is contrary to a charge-density wave (CDW) picture. In CDWs, the sum of electrostatic energies provides the gain, while some kinetic energy is lost. This point is further illustrated by a model polyacetylene calculation.

3. We calculate (chapter 4) the relative core level shifts of two inequivalent adatoms on 3×3 Sn/Ge(111), and find a value which compares fairly well with experiment. The "up" adatoms core level, in particular, is found to be deeper than that of "down" adatoms, pointing to the fact that the difference between the two is mostly hybridization, but not total charge (that would give the opposite sign to the shift).

4. We also calculate (chapter 4) the work function of Sn/Ge(111), both in the $\sqrt{3} \times \sqrt{3}R30°$ undistorted (unstable) state, and in the 3×3, "1 up" distorted state. The calculated shift is extremely small, indicating a negligible change of surface dipole, in full agreement with the lack of true up-down charge transfer also suggested by the core level analysis.

5. We investigate (chapter 5) the effects of magnetism on the Sn/Ge(111) system, in particular we explore the possibility that a magnetic phase might show good nesting properties and/or exhibit insulating character. The answer is negative, and we conclude that magnetism is only of secondary importance for this surface.

6. We calculate (chapter 6) the effect of strain on the state of a surface like Sn/Ge(111), and obtain our main surprise. The 3×3 distortion disappears with large compression, and also with large tension. However the Sn adatom geometry, in particular its height over the second-layer Ge substrate atom, does not change continuously. The adatom

has two stable positions, up (U) and down (D). Under tensile strain, all adatoms are D (0U). At zero strain, one out of three is up (1U), and for increasing compressive strain we have 2U, and finally 3U (all adatoms up, $\sqrt{3} \times \sqrt{3}R30°$ periodicity). The U and D states appear as two different "valences" of Sn, and thus the Sn/Ge(111) and similar surfaces could be seen as mixed valence systems.

7. We have identified (chapter 7) a novel fractional charge defect in the Phaneuf-Webb model of clean Ge(111) above 540 K. The resulting fractional doping is held responsible for the weak metallic behavior seen on this surface by EELS and photoemission.

Chapter 1

Computational methods

1.1 Density functional theory

The *density functional theory* (DFT) [1, 2, 3, 4] is a general scheme which can be used to reduce a quantum-mechanical, many-body problem to an effective one-electron problem, that can be solved much more easily.

Its basic theorem [1, 4] states that in the adiabatic approximation, the energy E of the electronic ground state is a unique, universal functional of the electron density matrix $\underline{\underline{n}}(\mathbf{r})$, and that we can write [1, 3, 4]

$$E\left[\underline{\underline{n}}(\mathbf{r})\right] = T_0\left[\underline{\underline{n}}(\mathbf{r})\right] + E_H\left[\underline{\underline{n}}(\mathbf{r})\right] + E_{en}\left[\underline{\underline{n}}(\mathbf{r})\right] + E_{nn} + E_{xc}\left[\underline{\underline{n}}(\mathbf{r})\right] \qquad (1.1)$$

where the right-hand terms have the following meanings:

- $T_0\left[\underline{\underline{n}}(\mathbf{r})\right]$ is the kinetic energy of a system of *non-interacting* electrons

$$T_0\left[\underline{\underline{n}}(\mathbf{r})\right] = -\frac{\hbar^2}{2m} \sum_{\sigma=+,-} \sum_i f_{i,\sigma} \int \psi_{i,\sigma}^*(\mathbf{r}) \nabla^2 \psi_{i,\sigma}(\mathbf{r}) \, d\mathbf{r} \qquad (1.2)$$

where the $\psi_{i,\sigma}(\mathbf{r})$ are single-particle electronic wavefunctions, σ being the spin ($\sigma = +$ for spin up, $\sigma = -$ for spin down), and the $f_{i,\sigma}$ are their respective occupation numbers. The corresponding electron density is

$$n(\mathbf{r}) = n_+(\mathbf{r}) + n_-(\mathbf{r}) \qquad (1.3)$$

where

$$n_\sigma(\mathbf{r}) = \sum_i f_{i,\sigma} \left|\psi_{i,\sigma}(\mathbf{r})\right|^2 . \qquad (1.4)$$

- $E_H\left[\underline{\underline{n}}(\mathbf{r})\right]$ is the (Hartree) interaction energy between electrons

$$E_H\left[\underline{\underline{n}}(\mathbf{r})\right] = \frac{1}{2}\frac{e^2}{4\pi\varepsilon_0}\int\frac{n(\mathbf{r})n(\mathbf{r}')}{|\mathbf{r}-\mathbf{r}'|}\,\mathrm{d}\mathbf{r}\,\mathrm{d}\mathbf{r}' \tag{1.5}$$

i.e., the classical electrostatic energy of the electron density $n(\mathbf{r})$.

- $E_{en}\left[\underline{\underline{n}}(\mathbf{r})\right]$ is the interaction energy between electrons and nuclei

$$E_{en}\left[\underline{\underline{n}}(\mathbf{r})\right] = \sum_{\sigma=+,-}\int v_\sigma(\mathbf{r})n_\sigma(\mathbf{r})\,\mathrm{d}\mathbf{r} \tag{1.6}$$

where

$$v_\sigma(\mathbf{r}) = \sum_I V_I(\mathbf{r}-\mathbf{R}_I) - \mu_B s(\sigma)B(\mathbf{r}) \tag{1.7}$$

is the total potential exerted by nuclei, plus a spin-dependent Zeeman term (usually zero); $\mathbf{R}_I$ is the position of the I-th nucleus, and $V_I(\mathbf{r})$ is its electron-nucleus potential, while $\mu_B = e\hbar/2m$ is the Bohr magneton, $s(+) = 1$, and $s(-) = -1$.

- E_{nn} is the interaction energy between nuclei

$$E_{nn} = \frac{1}{2}\frac{e^2}{4\pi\varepsilon_0}\sum_{I,J\neq I}\frac{Z_I Z_J}{|\mathbf{R}_I-\mathbf{R}_J|} \tag{1.8}$$

that, as long as we consider the electronic problem for a fixed nuclear configuration, is just an additive constant.

- $E_{xc}\left[\underline{\underline{n}}(\mathbf{r})\right]$ is the *exchange and correlation* energy, coming from two sources:

  - The difference between the true electron-electron interaction and the Hartree energy, equation (1.5), which incorrectly includes the interaction of each electron with itself.

  - The difference between the kinetic energy of a system of *interacting* electrons and the non-interacting expression of equation (1.2).

In other words, $E_{xc}\left[\underline{\underline{n}}(\mathbf{r})\right]$ is defined by the following relation:

$$T + V = T_0\left[\underline{\underline{n}}(\mathbf{r})\right] + \left(E_H\left[\underline{\underline{n}}(\mathbf{r})\right] + E_{en}\left[\underline{\underline{n}}(\mathbf{r})\right] + E_{nn}\right) + E_{xc}\left[\underline{\underline{n}}(\mathbf{r})\right] \tag{1.9}$$

where T and V are the true kinetic and potential energy of the system.

No exact expression is known for $E_{xc}[\underline{n}(\mathbf{r})]$; in the *local-spin-density* approximation (LSDA) [3, 4], we assume that this functional can locally be approximated by its value for a *uniform* electron gas, that is, we let

$$E_{xc}[\underline{n}(\mathbf{r})] = \int \varepsilon_{xc}\left(n_+(\mathbf{r}), n_-(\mathbf{r})\right) n(\mathbf{r})\, d\mathbf{r} \tag{1.10}$$

$\varepsilon_{xc}(n_+, n_-)$ being the exchange-correlation energy per electron of a uniform electron gas of spin-up density n_+ and spin-down density n_-: expressions for it are available in the literature [5, 6, 7].

When effects of spin are neglected, the name LDA (local-density approximation) is used in place of LSDA.

Now, if we define

$$v_\sigma^{xc}(\mathbf{r}) = \frac{\delta E_{xc}[\underline{n}(\mathbf{r})]}{\delta n_\sigma(\mathbf{r})} \tag{1.11}$$

we can see that the system is equivalent to a system of non-interacting electrons whose single-particle Schrödinger equation is

$$H_{KS}\psi_{i,\sigma}(\mathbf{r}) = \left(-\frac{\hbar^2}{2m}\nabla^2 + V_\sigma^{KS}(\mathbf{r})\right)\psi_{i,\sigma}(\mathbf{r}) = \varepsilon_{i,\sigma}\psi_{i,\sigma}(\mathbf{r}) \tag{1.12}$$

$$V_\sigma^{KS}(\mathbf{r}) = \frac{e^2}{4\pi\varepsilon_0}\int \frac{n(\mathbf{r}')}{|\mathbf{r} - \mathbf{r}'|}\, d\mathbf{r}' + v_\sigma(\mathbf{r}) + v_\sigma^{xc}(\mathbf{r}) \tag{1.13}$$

the electron density $n(\mathbf{r})$ being given by equation (1.3) with the occupation numbers $f_{i,\sigma} = \mathcal{F}(\varepsilon_{i,\sigma})$, where $\mathcal{F}(E)$ is the Fermi distribution; the Fermi energy is determined by the sum rule $\sum_{i,\sigma} f_{i,\sigma} = N_e$, where N_e is the number of electrons in the system.

The above equation is called *Kohn-Sham* equation [3, 4]; $v_\sigma^{xc}(\mathbf{r})$ is the (spin-dependent) *exchange-correlation potential*. Its expression within the LSDA is

$$v_\sigma^{xc}(\mathbf{r}) = \mu_\sigma^{xc}\left(n_+(\mathbf{r}), n_-(\mathbf{r})\right) \tag{1.14}$$

where $\mu_\sigma^{xc}(n_+, n_-)$ is the exchange-correlation contribution to the chemical potential for the uniform electron gas

$$\mu_\sigma^{xc}(n_+, n_-) = \frac{d\left((n_+ + n_-)\varepsilon_{xc}(n_+, n_-)\right)}{dn_\sigma}. \tag{1.15}$$

The total energy can be written as

$$E = -\frac{\hbar^2}{2m}\sum_{i,\sigma} f_{i,\sigma}\int \psi_{i,\sigma}^*(\mathbf{r})\nabla^2\psi_{i,\sigma}(\mathbf{r})\, d\mathbf{r} + \frac{1}{2}\frac{e^2}{4\pi\varepsilon_0}\int \frac{n(\mathbf{r})n(\mathbf{r}')}{|\mathbf{r} - \mathbf{r}'|}\, d\mathbf{r}\, d\mathbf{r}' +$$

$$+ \sum_\sigma \int v_\sigma(\mathbf{r}) n_\sigma(\mathbf{r}) \, \mathrm{d}\mathbf{r} + E_{xc}\big[\underline{n}(\mathbf{r})\big] + E_{nn} =$$

$$= \sum_{i,\sigma} f_{i,\sigma} \varepsilon_{i,\sigma} - \frac{1}{2} \frac{e^2}{4\pi\varepsilon_0} \int \frac{n(\mathbf{r})n(\mathbf{r}')}{|\mathbf{r}-\mathbf{r}'|} \, \mathrm{d}\mathbf{r} \, \mathrm{d}\mathbf{r}' + E_{xc}\big[\underline{n}(\mathbf{r})\big] -$$

$$- \sum_\sigma \int v_\sigma^{xc}(\mathbf{r}) n_\sigma(\mathbf{r}) \, \mathrm{d}\mathbf{r} + E_{nn} \tag{1.16}$$

and in the LSDA

$$E = \sum_{i,\sigma} f_{i,\sigma} \varepsilon_{i,\sigma} - \frac{1}{2} \frac{e^2}{4\pi\varepsilon_0} \int \frac{n(\mathbf{r})n(\mathbf{r}')}{|\mathbf{r}-\mathbf{r}'|} \, \mathrm{d}\mathbf{r} \, \mathrm{d}\mathbf{r}' + \tag{1.17}$$

$$+ \sum_\sigma \int \left[\varepsilon_{xc}\left(n_+(\mathbf{r}), n_-(\mathbf{r}) \right) - \mu_\sigma^{xc}\left(n_+(\mathbf{r}), n_-(\mathbf{r}) \right) \right] n_\sigma(\mathbf{r}) \, \mathrm{d}\mathbf{r} + E_{nn}.$$

As we see, the Kohn-Sham Hamiltonian H_{KS} depends on the electron spin-up and spin-down densities, which in turn depend on the wavefunctions $\psi_{i,\sigma}(\mathbf{r})$: thus the Kohn-Sham equations must be solved self-consistently, by guessing suitable starting densities $n_\sigma^{(0)}(\mathbf{r})$ (a superposition of atomic orbitals is usually a good starting point) and generating successive approximations $n_\sigma^{(i)}(\mathbf{r})$ by repeatedly solving the equations, until the desired accuracy is achieved. A number of methods for accelerating the convergence rate are known, e.g., the Broyden [8, 9] and Davidson [10] methods.

We are thus able to solve the electronic problem for any fixed ionic configuration $\mathbf{R}$: to find the ground state of the system, we must look for the value of $\mathbf{R}$ that yields the minimum value of the total energy E. The simplest way to obtain the optimal ionic configuration is to start with a trial configuration, evaluate forces, move each atom proportionally to the force acting on it, and repeat this procedure until an equilibrium configuration is reached (some care is required to avoid falling into a *local* minimum).

Forces acting on nuclei can be evaluated through the Hellmann-Feynman formula [11]:

$$F_\lambda = -\frac{\partial E}{\partial \lambda} = -\langle \psi | \frac{\partial H}{\partial \lambda} | \psi \rangle \tag{1.18}$$

where λ is one of a set of parameters describing the nuclear configuration, usually the Cartesian coordinates of nuclear positions.

To obtain more accurate results, the local-(spin-)density approximation is often corrected by using a functional of the *generalized gradient* approximation (GGA) type, that is, the exchange-correlation energy is expressed as a local function of $n(\mathbf{r})$ *and* of its gradient:

$$E_{xc}\big[\underline{n}(\mathbf{r})\big] = \int f\left(n_+(\mathbf{r}), n_-(\mathbf{r}), \nabla n_+(\mathbf{r}), \nabla n_-(\mathbf{r})\right) \, \mathrm{d}\mathbf{r} \tag{1.19}$$

where $f(n_+, n_-, \nabla n_+, \nabla n_-)$ is some suitable function. This approximation is also called a *gradient-corrected* L(S)DA. In this work, we used mainly the functional by Perdew, Burke, and Ernzerhof (PBE) [12]:

$$E_x\big[\underline{n}(\mathbf{r})\big] = \sum_{\sigma=+,-} \int \varepsilon_x\left(2n_\sigma(\mathbf{r})\right) F(s_\sigma(\mathbf{r}))\, n_\sigma(\mathbf{r})\, d\mathbf{r} = \qquad (1.20)$$

$$= E_x^{LSDA}\big[\underline{n}(\mathbf{r})\big] + \sum_{\sigma=+,-} \int \varepsilon_x\left(2n_\sigma(\mathbf{r})\right) \left[F(s_\sigma(\mathbf{r})) - 1\right] n_\sigma(\mathbf{r})\, d\mathbf{r}$$

$$E_c\big[\underline{n}(\mathbf{r})\big] = E_c^{LSDA}\big[\underline{n}(\mathbf{r})\big] + \int H(n_+(\mathbf{r}), n_-(\mathbf{r}), t(\mathbf{r}))\, n(\mathbf{r})\, d\mathbf{r} \qquad (1.21)$$

where $\varepsilon_x(n) = \varepsilon_x(\frac{1}{2}n, \frac{1}{2}n)$ is the exchange energy per electron of the unpolarized electron gas, and

$$s_\sigma(\mathbf{r}) = \frac{1}{2(3\pi^2)^{1/3}} \frac{|\nabla n_\sigma(\mathbf{r})|}{n_\sigma(\mathbf{r})^{4/3}} \qquad (1.22)$$

$$t(\mathbf{r}) = \frac{1}{4}\left(\frac{\pi}{3}\right)^{1/6} \left(\frac{\hbar^2}{m} \frac{4\pi\varepsilon_0}{e^2}\right)^{1/2} \frac{1}{g(n_+(\mathbf{r}), n_-(\mathbf{r}))} \frac{|\nabla n(\mathbf{r})|}{n(\mathbf{r})^{7/6}} \qquad (1.23)$$

$$g(n_+, n_-) = 2^{-1/3}\left[\left(\frac{n_+}{n}\right)^{2/3} + \left(\frac{n_-}{n}\right)^{2/3}\right] \qquad (1.24)$$

$$F(s) = 1 + \kappa - \left(\kappa + \frac{\pi^2}{3}\beta s^2\right)^{-1} \qquad (1.25)$$

$$H(n_+, n_-, t) = \gamma \frac{m}{\hbar^2} \left(\frac{e^2}{4\pi\varepsilon_0}\right)^2 g(n_+, n_-)^3 \times$$

$$\times \log\left[1 + \frac{\beta}{\gamma} \frac{t^2 + A(n_+, n_-)t^4}{1 + A(n_+, n_-)t^2 + A(n_+, n_-)^2 t^4}\right] \qquad (1.26)$$

$$A(n_+, n_-) = \frac{\beta}{\gamma}\left[\exp\left(-\frac{1}{\gamma}\frac{m}{\hbar^2}\left(\frac{e^2}{4\pi\varepsilon_0}\right)^2 \frac{\varepsilon_c(n_+, n_-)}{g(n_+, n_-)^3}\right) - 1\right]^{-1} \qquad (1.27)$$

$$\kappa = 0.804 \qquad \gamma = \frac{1 - \log 2}{\pi^2} \qquad \beta = 0.066725. \qquad (1.28)$$

1.2 Pseudopotentials

It is well known (indeed, this fact constitutes the rationale for the periodic table of the elements) that a major role in determining the chemical properties of an atom is played by electrons in its outermost shell: this is because inner electrons have wavefunctions at much deeper energy levels and stay very close to the nucleus, and are thus substantially insensitive to the atom's environment.

Therefore, in the *frozen-core* approximation, electrons are partitioned into two sets: *core* and *valence* electrons, and it is assumed that the core electrons' wavefunctions are the same as for an isolated atom. The choice of valence electrons is somewhat arbitrary: one tries to pick as few of them as required to obtain reliable results, in order to reduce the computational cost. This implies that reliability of a given choice must be checked. Often, one picks just the s and p electrons from the outermost shell, that is, no more than 8 per atom.

A *pseudopotential* [13, 14] is an effective potential, obtained as the nuclear potential screened by core electrons: this is the potential seen, on the average, by valence electrons. Thus, in a pseudopotential calculation, valence eigenvalues are obtained as the *lowest* eigenvalues of the effective Hamiltonian containing the pseudopotential (often called a pseudo-Hamiltonian); the corresponding wavefunctions are not the true valence wavefunctions, and are thus called pseudo-wavefunctions. Valence electrons fill these pseudo-wavefunctions, while core electrons, in this formalism, are neglected.

Several methods for systematic, *ab initio* generation of pseudopotentials have then been developed [14, 15, 16, 17, 18]. Modern pseudopotentials [16, 17, 18] are calculated by choosing an atomic reference state (usually the ground state; other states can be used for particular applications), and imposing that the pseudopotential satisfies for that state a number of properties chosen so as to ensure maximum *transferability*, that is, that the generated pseudopotential can be used in as many different environments as possible.

The following properties are most frequently selected:

- Atomic pseudo-eigenvalues are equal to the corresponding true valence eigenvalues.

- Atomic pseudo-wavefunctions are strictly equal to the corresponding true valence wavefunctions beyond a chosen *core radius* r_c.

- The integral from 0 to r_c of the atomic pseudo-electron density is equal to the corresponding true electron density for each valence state (norm conservation).

- The logarithmic derivatives of atomic pseudo-wavefunctions and their first energy derivatives match those of the corresponding true wavefunctions at $r = r_c$.

Pseudopotentials are often *nonlocal*, that is, they depend on the angular momentum of the electron: such a potential is usually generated in the form

$$\hat{V}^{SL} = \sum_l V_l^{SL}(|\mathbf{r}|)\hat{P}_l \qquad (1.29)$$

where $\hat{P}_l = \sum_m |Y_{lm}\rangle\langle Y_{lm}|$ is the projector on angular momentum l, the $|Y_{lm}\rangle$ being spherical harmonics. This is called the "semilocal" form of the pseudopotential.

However, all the $V_l^{SL}(r)$ are equal to the true potential, and therefore to each other, for all r greater than the core radius r_c: the pseudopotential can thus be written as a local part, plus a short-ranged nonlocal one. One of the $V_l^{SL}(r)$ is usually taken as the local part: at large r, it must go as $-Ze^2/4\pi\varepsilon_0 r$, Z being the valence of the ion.

As we will show in section 1.3, pseudopotentials are often treated in momentum space; this requires evaluation of matrix elements with respect to plane waves $\langle e^{i\mathbf{k}\cdot\mathbf{r}}|\hat{V}|e^{i\mathbf{k}'\cdot\mathbf{r}}\rangle$, which in turn requires evaluation of integrals for each value of the pair $(\mathbf{k},\mathbf{k}')$. Kleinman and Bylander have shown [19] that by expressing the pseudopotential in an alternate form, each matrix element can be factored into a term depending on $\mathbf{k}$ and one depending on $\mathbf{k}'$ only, greatly reducing the number of integrals to evaluate.

Namely, if a nonlocal pseudopotential, in the semilocal form (1.29), has been generated for a reference state

$$|\psi^0\rangle = \sum_{l,m}|Y_{lm}\rangle\langle Y_{lm}|\psi^0\rangle = \sum_{l,m}|\psi^0_{lm}Y_{lm}\rangle \qquad (1.30)$$

where

$$\psi^0_{lm}(r) = \langle Y_{lm}|\psi^0\rangle = \int \psi^0(r,\theta,\phi)Y_{lm}(\theta,\phi)\,\mathrm{d}\cos\theta\,\mathrm{d}\phi \qquad (1.31)$$

we can rewrite it in the ("fully nonlocal") form

$$\hat{V}^{KB} = \sum_{l,m}|V^{KB}_{lm}Y_{lm}\rangle\langle Y_{lm}V^{KB}_{lm}| \qquad (1.32)$$

having let

$$V^{KB}_{lm}(r) = \frac{V_l^{SL}(r)\psi^0_{lm}(r)}{\langle Y_{lm}\psi^0_{lm}|V_l^{SL}|\psi^0_{lm}Y_{lm}\rangle^{1/2}} = \frac{V_l^{SL}(r)\psi^0_{lm}(r)}{\left(\int \psi^0_{lm}{}^*(r')V_l^{SL}(r')\psi^0_{lm}(r')r'^2\,\mathrm{d}r'\right)^{1/2}}. \qquad (1.33)$$

This potential is equal to $\hat{V}^{SL}$ at $|\psi^0\rangle$, for

$$\begin{aligned}
\hat{V}^{KB}|\psi^0\rangle &= \sum_{l,m}\frac{|V_l^{SL}\psi^0_{lm}Y_{lm}\rangle\langle Y_{lm}\psi^0_{lm}V_l^{SL}|\psi^0\rangle}{\langle Y_{lm}\psi^0_{lm}|V_l^{SL}|\psi^0_{lm}Y_{lm}\rangle} = \\
&= \sum_{l,m}V_l^{SL}(r)|\psi^0_{lm}Y_{lm}\rangle = \hat{V}^{SL}|\psi^0\rangle. \qquad (1.34)
\end{aligned}$$

15

Using this form, plane-wave matrix elements can be factored as such:

$$\left\langle e^{i\mathbf{k}\cdot\mathbf{r}} \left| \hat{V}^{KB} \right| e^{i\mathbf{k}'\cdot\mathbf{r}} \right\rangle = \sum_{l,m} \left\langle e^{i\mathbf{k}\cdot\mathbf{r}} \left| V_{lm}^{KB} Y_{lm} \right\rangle \left\langle Y_{lm} V_{lm}^{KB} \right| e^{i\mathbf{k}'\cdot\mathbf{r}} \right\rangle =$$

$$= \sum_{l,m} 4\pi Y_{lm}\left(\frac{\mathbf{k}}{|\mathbf{k}|}\right) \int j_l\left(|\mathbf{k}|\,r\right) V_{lm}^{KB}(r) r^2 \,\mathrm{d}r \times$$

$$\times\, 4\pi Y_{lm}^*\left(\frac{\mathbf{k}'}{|\mathbf{k}'|}\right) \int j_l\left(|\mathbf{k}'|\,r'\right) V_{lm}^{KB}(r') r'^2 \,\mathrm{d}r' \qquad (1.35)$$

where $j_l(x)$ is the spherical Bessel function of order l [20, 21].

To express it efficiently in Fourier space, it is also advisable that a pseudopotential is as smooth as possible. Methods for generating very smooth pseudopotentials have been presented [18, 22].

1.3 Plane-wave expansion

To solve the Kohn-Sham equations numerically for a given system, it is especially suited to express them in momentum space, expanding wavefunctions in terms of plane waves [23]. Crucial for the computational efficiency of this formalism is the *Fast Fourier Transform* (FFT) technique [24, 25], which allows to transform data efficiently between meshes of real- and momentum-space points.

We start by imposing periodic boundary conditions: thus, by Bloch's theorem [26], we can choose a set of wavefunctions of the form $\psi_{i,\sigma\mathbf{k}}(\mathbf{r}) = e^{i\mathbf{k}\cdot\mathbf{r}}\phi_{i,\sigma\mathbf{k}}(\mathbf{r})$, where $\phi_{i,\sigma\mathbf{k}}(\mathbf{r})$ is periodic, while $\mathbf{k}$ is a vector in the first Brillouin zone. Bloch wavefunctions can be expanded in Fourier series as follows:

$$\psi_{i,\sigma\mathbf{k}}(\mathbf{r}) = e^{i\mathbf{k}\cdot\mathbf{r}}\phi_{i,\sigma\mathbf{k}}(\mathbf{r}) = e^{i\mathbf{k}\cdot\mathbf{r}}\sum_{\mathbf{G}} e^{i\mathbf{G}\cdot\mathbf{r}}\phi_{i,\sigma\mathbf{k}}(\mathbf{G}) \qquad (1.36)$$

$$\phi_{i,\sigma\mathbf{k}}(\mathbf{G}) = \frac{1}{\Omega}\int_{cell} e^{-i\mathbf{G}\cdot\mathbf{r}}\phi_{i,\sigma\mathbf{k}}(\mathbf{r})\,\mathrm{d}\mathbf{r} \simeq \frac{1}{N_{mesh}}\sum_{\mathbf{r}} e^{-i\mathbf{G}\cdot\mathbf{r}}\phi_{i,\sigma\mathbf{k}}(\mathbf{r}) \qquad (1.37)$$

where the sum over $\mathbf{r}$ ranges over a mesh of N_{mesh} points covering the unit cell.

The corresponding electron density is

$$n(\mathbf{r}) = n_+(\mathbf{r}) + n_-(\mathbf{r}) \qquad (1.38)$$

$$n_\sigma(\mathbf{r}) = \sum_{\mathbf{k}} w_{\mathbf{k}} \sum_i f_{i,\sigma\mathbf{k}} \left|\psi_{i,\sigma\mathbf{k}}(\mathbf{r})\right|^2 = \sum_{\mathbf{k}} w_{\mathbf{k}} \sum_i f_{i,\sigma\mathbf{k}} \left|\phi_{i,\sigma\mathbf{k}}(\mathbf{r})\right|^2 \qquad (1.39)$$

where the finite sum over **k** approximates an integral over the Brillouin zone; each **k** point is assigned a suitably chosen weight $w_\mathbf{k}$. The condition $\sum_\mathbf{k} w_\mathbf{k} = 1$ must hold for normalization.

The sum rule for the occupation numbers $f_{i,\sigma\mathbf{k}}$ is thus

$$\sum_{\sigma,\mathbf{k}} w_\mathbf{k} \sum_i f_{i,\sigma\mathbf{k}} = N_e \tag{1.40}$$

where N_e is the number of electrons per unit cell.

Systematic methods have been developed [27, 28, 29, 30, 31] to choose good sets of **k** points and corresponding weights: it is found that accurate results can be obtained even with very small, but carefully chosen, sets. Taking advantage of the symmetries of the system, we can often reduce to sampling the *irreducible* Brillouin zone (IBZ) only, which can be a very small part (as small as 1/48 when full cubic symmetry holds) of the whole first Brillouin zone.

When studying a metallic system, the technique of *smearing* the states near the Fermi energy must be used [32], for example, a Gaussian density is associated to each state, and the occupation number is set to the area below E_F:

$$f_{i,\sigma\mathbf{k}} = \frac{1}{\Delta\sqrt{\pi}} \int_{-\infty}^{E_F} e^{-(E-\varepsilon_{i,\sigma\mathbf{k}})^2/\Delta^2} \, \mathrm{d}E \tag{1.41}$$

having put E_F at the level which gives the correct sum. Otherwise, due to the use of a finite set of **k** points, numerical problems can show up because of abrupt occupation numbers jumps.

It is clear that $n(\mathbf{r})$ is periodic over the unit cell: thus it can also be expanded in Fourier series as

$$n(\mathbf{r}) = \sum_\mathbf{G} e^{i\mathbf{G}\cdot\mathbf{r}} n(\mathbf{G}), \qquad n(\mathbf{G}) = \frac{1}{N_{mesh}} \sum_\mathbf{r} e^{-i\mathbf{G}\cdot\mathbf{r}} n(\mathbf{r}) \tag{1.42}$$

and similar formulas apply to all periodic observables.

To truncate the Fourier expansions to a finite number of **G** points, we observe that, assuming a sufficient degree of regularity in the quantities involved in our calculation, their Fourier coefficients tend to zero as $|\mathbf{G}| \to \infty$. Thus, we do as small an error as we want if we restrict to the **G** vectors such that $|\mathbf{G}|$ is less than a suitably chosen *cutoff wavevector* G_{cut}. The latter is usually expressed in terms of the corresponding *cutoff energy*

$$E_{cut} = \frac{\hbar^2}{2m} G_{cut}^2 \tag{1.43}$$

where m is the mass of the electron.

17

We can thus choose the smallest rectangular momentum-space mesh enclosing the cutoff sphere; then, for the real-space mesh, we set the spacing so as to obtain the same number of points. The accuracy of the computation can be sistematically improved, of course at the expense of more computer time, by increasing the number of **k** points and/or the cutoff energy. A discussion on how to choose them is given in Ref. [33].

A substantial time saving can be obtained by using pseudopotentials: not only the number of wavefunctions to be considered is made significantly smaller (very often only 4 per atom, while large elements have several tens of electrons), but wavefunctions are also smoother, thus allowing us to represent them accurately with a smaller cutoff. As a result, the computational time can be reduced by several orders of magnitude.

Therefore, we consider the general case of a nonlocal ion-electron interaction (pseudo-) potential $\hat{V}_s$, where s labels the atomic species: we denote by τ_s the set of I such that the I-th atom is of species s. Denoting with Z_s the valence of an ion of species s, the total number of valence electrons per cell will thus be

$$N_e = \sum_I Z_{s(I)} = \sum_s N_s Z_s \qquad (1.44)$$

N_s being the number of atoms of species s, while $s(I)$ is the species of the I-th ion.

Fourier components of the quantities of interest are as follows [23]:

- Kinetic energy:

$$-\frac{\hbar^2}{2m} \sum_{\sigma,\mathbf{k}} w_{\mathbf{k}} \sum_i f_{i,\sigma\mathbf{k}} \int \psi_{i,\sigma\mathbf{k}}^*(\mathbf{r}) \nabla^2 \psi_{i,\sigma\mathbf{k}}(\mathbf{r}) \, d\mathbf{r} =$$

$$= \frac{\hbar^2}{2m} \Omega \sum_{\sigma,\mathbf{k}} w_{\mathbf{k}} \sum_{i,\mathbf{G}} f_{i,\sigma\mathbf{k}} \, |\mathbf{k}+\mathbf{G}|^2 \, |\phi_{i,\sigma\mathbf{k}}(\mathbf{G})|^2. \qquad (1.45)$$

- Hartree electron-electron interaction energy:

$$\frac{1}{2} \frac{e^2}{4\pi\varepsilon_0} \int \frac{n(\mathbf{r})n(\mathbf{r}')}{|\mathbf{r}-\mathbf{r}'|} \, d\mathbf{r} \, d\mathbf{r}' = \frac{1}{2} \frac{e^2}{4\pi\varepsilon_0} \Omega \sum_{\mathbf{G}} \frac{4\pi}{\mathbf{G}^2} n(-\mathbf{G})n(\mathbf{G}). \qquad (1.46)$$

Note that the term with $\mathbf{G} = 0$ is divergent (it cancels out together with other terms, shown below):

$$\left[\frac{1}{2} \frac{e^2}{4\pi\varepsilon_0} \Omega \frac{4\pi}{\mathbf{G}^2} n(0)^2 \right]_{\mathbf{G}=0} = \left[\frac{1}{2} \frac{e^2}{4\pi\varepsilon_0} \Omega \frac{4\pi}{\mathbf{G}^2} \left(\frac{1}{\Omega} \int n(\mathbf{r}) \, d\mathbf{r} \right)^2 \right]_{\mathbf{G}=0} =$$

$$= \left[\frac{1}{2} \frac{e^2}{4\pi\varepsilon_0} \frac{4\pi}{\mathbf{G}^2} \frac{N_e^2}{\Omega} \right]_{\mathbf{G}=0}. \qquad (1.47)$$

18

- Electron-electron exchange-correlation energy: in the LSDA

$$\int \varepsilon_{xc}\left(n_+(\mathbf{r}), n_-(\mathbf{r})\right) n(\mathbf{r})\, \mathrm{d}\mathbf{r} = \tag{1.48}$$

$$= \sum_{\mathbf{G}} n(\mathbf{G}) \int e^{i\mathbf{G}\cdot\mathbf{r}} \varepsilon_{xc}\left(n_+(\mathbf{r}), n_-(\mathbf{r})\right)\, \mathrm{d}\mathbf{r} = \Omega \sum_{\mathbf{G}} \varepsilon_{xc}(-\mathbf{G}) n(\mathbf{G})$$

where $\varepsilon_{xc}(\mathbf{G})$ must be recomputed at each step by Fourier-transforming $\varepsilon_{xc}\left(n_+(\mathbf{r}), n_-(\mathbf{r})\right)$ for the current electron density.

- Electron-ion energy: as mentioned in section 1.2, we write the pseudopotential as the sum of a local part and a nonlocal, short-ranged one.

The former gives

$$\sum_{\sigma,\mathbf{k}} w_{\mathbf{k}} \sum_i f_{i,\sigma\mathbf{k}} \int \psi^*_{i,\sigma\mathbf{k}}(\mathbf{r}) \left(\sum_I V^{loc}_{s(I)}(\mathbf{r} - \mathbf{R}_I)\right) \psi_{i,\sigma\mathbf{k}}(\mathbf{r})\, \mathrm{d}\mathbf{r} = \tag{1.49}$$

$$= \sum_s \int n(\mathbf{r}) \sum_{I\in\tau_s} V^{loc}_s(\mathbf{r} - \mathbf{R}_I)\, \mathrm{d}\mathbf{r} = \Omega \sum_{s,\mathbf{G}} S_s(\mathbf{G}) V^{loc}_s(-\mathbf{G}) n(\mathbf{G})$$

having defined the *structure factors*

$$S_s(\mathbf{G}) = \sum_{I\in\tau_s} e^{i\mathbf{G}\cdot\mathbf{R}_I} \tag{1.50}$$

and denoting with τ_s the set of I's such that the I-th atom is of species s. Again, the term with $\mathbf{G} = 0$ is divergent, because $V^{loc}_s(\mathbf{r})$ must go as $-Z_s e^2/4\pi\varepsilon_0 |\mathbf{r}|$ for large $\mathbf{r}$:

$$\Omega \sum_s S_s(0) V^{loc}_s(0) n(0) = \frac{N_e}{\Omega} \sum_s \sum_{I\in\tau_s} e^0 \int V^{loc}_s(\mathbf{r})\, \mathrm{d}\mathbf{r} = \tag{1.51}$$

$$= \frac{N_e N_s}{\Omega} \sum_s \int \left(V^{loc}_s(\mathbf{r}) + Z_s \frac{e^2}{4\pi\varepsilon_0} \frac{1}{|\mathbf{r}|}\right)\, \mathrm{d}\mathbf{r} - \left[\frac{e^2}{4\pi\varepsilon_0} \frac{4\pi}{\mathbf{G}^2} \frac{N_e^2}{\Omega}\right]_{\mathbf{G}=0}.$$

The nonlocal part may be expressed in the semilocal form (1.29), in which case we obtain

$$\sum_{\sigma,\mathbf{k}} w_{\mathbf{k}} \sum_i f_{i,\sigma\mathbf{k}} \int \psi^*_{i,\sigma\mathbf{k}}(\mathbf{r}) \left(\sum_{I,l} V^{SL}_{s(I),l}(|\mathbf{r} - \mathbf{R}_I|) \hat{P}_l\right) \psi_{i,\sigma\mathbf{k}}(\mathbf{r})\, \mathrm{d}\mathbf{r} = \cdot$$

$$= \Omega \sum_{\sigma,\mathbf{k}} w_{\mathbf{k}} \sum_{\mathbf{G},\mathbf{G}'} \left(\sum_i f_{i,\sigma\mathbf{k}} \phi^*_{i,\sigma\mathbf{k}}(\mathbf{G}) \phi_{i,\sigma\mathbf{k}}(\mathbf{G}') \times\right.$$

$$\left.\times \sum_s S_s(\mathbf{G}' - \mathbf{G}) V^{NL}_s(\mathbf{k} + \mathbf{G}, \mathbf{k} + \mathbf{G}')\right) \tag{1.52}$$

having defined

$$V_s^{NL}(\mathbf{K}, \mathbf{K}') = \frac{1}{\Omega} \int e^{-i\mathbf{K}\cdot\mathbf{r}} \left(\sum_l V_{s,l}^{SL}(|\mathbf{r}|)\hat{P}_l \right) e^{i\mathbf{K}'\cdot\mathbf{r}} \, d\mathbf{r} =$$

$$= \frac{1}{\Omega} \sum_l (2l+1) P_l(\cos\omega) F_{s,l}^{SL}(\mathbf{K}, \mathbf{K}') \qquad (1.53)$$

$$F_{s,l}^{SL}(\mathbf{K}, \mathbf{K}') = 4\pi \int V_{s,l}^{SL}(r) j_l(|\mathbf{K}| r) j_l(|\mathbf{K}'| r) r^2 \, dr \qquad (1.54)$$

where $\cos\omega = \mathbf{K}\cdot\mathbf{K}'/(|\mathbf{K}|\,|\mathbf{K}'|)$, the $P_l(x)$ are the Legendre polynomials, and the $j_l(x)$ are the spherical Bessel functions [20, 21].

A more efficient way is to use the Kleinman-Bylander form (1.32): in this case we get (see section 1.2)

$$V_s^{NL}(\mathbf{K}, \mathbf{K}') = \frac{1}{\Omega} \int e^{-i\mathbf{K}\cdot\mathbf{r}} \left(\sum_{l,m} \left| V_{s,lm}^{KB} Y_{lm} \right\rangle \left\langle Y_{lm} V_{s,lm}^{KB} \right| \right) e^{i\mathbf{K}'\cdot\mathbf{r}} \, d\mathbf{r} =$$

$$= \frac{1}{\Omega} \sum_{l,m} Y_{lm}^* \left(\frac{\mathbf{K}}{|\mathbf{K}|} \right) Y_{lm} \left(\frac{\mathbf{K}'}{|\mathbf{K}'|} \right) F_{s,lm}^{KB}(\mathbf{K}) F_{s,lm}^{KB}(\mathbf{K}') \qquad (1.55)$$

where

$$F_{s,lm}^{KB}(\mathbf{K}) = 4\pi \int j_l(|\mathbf{K}| r) V_{s,lm}^{KB}(r) r^2 \, dr. \qquad (1.56)$$

The nonlocal energy term (1.52) is thus most efficiently evaluated by recasting it into the equivalent form

$$\sum_{\sigma,\mathbf{k}} w_{\mathbf{k}} \sum_{i,I,l,m} f_{i,\sigma\mathbf{k}} \left| \sum_{\mathbf{G}} \phi_{i,\sigma\mathbf{k}}(\mathbf{G}) e^{i\mathbf{G}\cdot\mathbf{R}_I} Y_{lm} \left(\frac{\mathbf{k}+\mathbf{G}}{|\mathbf{k}+\mathbf{G}|} \right) F_{s(I),lm}^{KB}(\mathbf{k}+\mathbf{G}) \right|^2$$

$$(1.57)$$

which avoids performing the double summation over $\mathbf{G}, \mathbf{G}'$.

- Ion-ion interaction term:

$$E_{nn} = \frac{1}{2} \frac{e^2}{4\pi\varepsilon_0} \left(\sum_{\substack{I\in cell \\ J\neq I}} \frac{Z_{s(I)} Z_{s(J)}}{|\mathbf{R}_I - \mathbf{R}_J|} - \frac{N_e^2}{\Omega} \int \frac{1}{|\mathbf{r}|} \, d\mathbf{r} \right) + \left[\frac{1}{2} \frac{e^2}{4\pi\varepsilon_0} \frac{4\pi}{\mathbf{G}^2} \frac{N_e^2}{\Omega} \right]_{\mathbf{G}=0}$$

$$(1.58)$$

having added and subtracted the energy of a neutralizing uniform charge density $-N_e e/\Omega$. The sum over J ranges over the whole infinite crystal.

The term in parentheses can be evaluated via standard Ewald-sum techniques: since it doesn't enter Kohn-Sham equations, it is computed just once for each given configuration of ions.

20

As we see, the three divergent terms exactly cancel each other. Therefore, the Kohn-Sham equations can be written as

$$\sum_{\mathbf{G}'} \left(|\mathbf{k} + \mathbf{G}'|^2\, \delta_{\mathbf{G}\mathbf{G}'} + V_{\sigma\mathbf{k}}^{KS}(\mathbf{G}, \mathbf{G}') \right) \phi_{i,\sigma\mathbf{k}}(\mathbf{G}') = \varepsilon_{i,\sigma\mathbf{k}}\phi_{i,\sigma\mathbf{k}}(\mathbf{G}) \qquad (1.59)$$

where

$$V_{\sigma\mathbf{k}}^{KS}(\mathbf{G}, \mathbf{G}') = v_H(\mathbf{G}' - \mathbf{G}) + v_\sigma^{xc}(\mathbf{G} - \mathbf{G}') + \qquad (1.60)$$
$$+ \sum_s S_s(\mathbf{G}' - \mathbf{G}) \left(V_s^{loc}(\mathbf{G} - \mathbf{G}') + V_s^{NL}(\mathbf{k} + \mathbf{G}, \mathbf{k} + \mathbf{G}') \right)$$

having let

$$v_H(\mathbf{G}) = \frac{e^2}{4\pi\varepsilon_0} \frac{4\pi}{\mathbf{G}^2} n(-\mathbf{G}) \qquad (1.61)$$

for $\mathbf{G} \neq 0$, and $v_H(0) = V_s^{loc}(0) = 0$.

Note that equations for different σ's and $\mathbf{k}$'s are uncorrelated, so that the system reduces into many subsystems to be solved separately. The only point in which different σ's and $\mathbf{k}$'s interact is when the electron density $n(\mathbf{G})$ is computed.

The total energy is given by

$$E = \frac{\hbar^2}{2m}\Omega \sum_{\sigma,\mathbf{k}} w_\mathbf{k} \sum_{i,\mathbf{G}} f_{i,\sigma\mathbf{k}} |\mathbf{k} + \mathbf{G}|^2 |\phi_{i,\sigma\mathbf{k}}(\mathbf{G})|^2 + \frac{1}{2}\Omega \sum_{\mathbf{G}\neq 0} v_H(\mathbf{G})n(\mathbf{G}) +$$
$$+ \Omega \sum_{s,\mathbf{G}\neq 0} S_s(\mathbf{G})V_s^{loc}(-\mathbf{G})n(\mathbf{G}) + \Omega \sum_{\sigma,\mathbf{k}} w_\mathbf{k} \times$$
$$\times \sum_{\mathbf{G},\mathbf{G}'} \left(\sum_i f_{i,\sigma\mathbf{k}}\phi_{i,\sigma\mathbf{k}}^*(\mathbf{G})\phi_{i,\sigma\mathbf{k}}(\mathbf{G}') \sum_s S_s(\mathbf{G}' - \mathbf{G})V_s^{NL}(\mathbf{k} + \mathbf{G}, \mathbf{k} + \mathbf{G}') \right) +$$
$$+ E_{xc}\left[\underline{n}(\mathbf{G})\right] + N_e \sum_s N_s\alpha_s + \gamma_{Ewald} =$$
$$= \sum_{\sigma,\mathbf{k}} w_\mathbf{k} \sum_i f_{i,\sigma\mathbf{k}}\varepsilon_{i,\sigma\mathbf{k}} - \frac{1}{2}\Omega \sum_{\mathbf{G}\neq 0} v_H(\mathbf{G})n(\mathbf{G}) + E_{xc}\left[\underline{n}(\mathbf{G})\right] -$$
$$- \Omega \sum_\sigma \sum_\mathbf{G} v_\sigma^{xc}(-\mathbf{G})n_\sigma(\mathbf{G}) + N_e \sum_s N_s\alpha_s + \gamma_{Ewald} \qquad (1.62)$$

where

$$\alpha_s = \frac{1}{\Omega} \int \left(V_s^{loc}(\mathbf{r}) + Z_s\frac{e^2}{4\pi\varepsilon_0}\frac{1}{|\mathbf{r}|} \right) d\mathbf{r} \qquad (1.63)$$

$$\gamma_{Ewald} = \frac{1}{2}\frac{e^2}{4\pi\varepsilon_0} \left(\sum_{\substack{I \in cell \\ J \neq I}} \frac{Z_{s(I)}Z_{s(J)}}{|\mathbf{R}_I - \mathbf{R}_J|} - \frac{N_e^2}{\Omega} \int \frac{1}{|\mathbf{r}|} d\mathbf{r} \right) \qquad (1.64)$$

21

and in the LSDA

$$E_{xc}\left[\underline{\underline{n}}(\mathbf{G})\right] = \Omega \sum_{\mathbf{G}} \varepsilon_{xc}(-\mathbf{G})n(\mathbf{G}). \tag{1.65}$$

E makes sense only once Kohn-Sham equations have been solved self-consistently. In practice, it is easily computed at each iteration, since this requires a relatively short time once $n(\mathbf{G})$ has been calculated, and differences between subsequent values are used to estimate convergence of the calculation.

The Hellmann-Feynman forces on ions [11] are given by:

- Pseudopotential, local part:

$$\begin{aligned}
\mathbf{F}_I^{loc} &= -\nabla_{\mathbf{R}_I}\left(\Omega \sum_{s,\mathbf{G}\neq 0} S_s(\mathbf{G})V_s^{loc}(-\mathbf{G})n(\mathbf{G})\right) = \\
&= -i\Omega \sum_{\mathbf{G}\neq 0} \mathbf{G}e^{i\mathbf{G}\cdot\mathbf{R}_I}V_{s(I)}^{loc}(-\mathbf{G})n(\mathbf{G}). \tag{1.66}
\end{aligned}$$

- Pseudopotential, nonlocal part:

$$\begin{aligned}
\mathbf{F}_I^{NL} &= -\nabla_{\mathbf{R}_I}\left[\Omega \sum_{\sigma,\mathbf{k}} w_{\mathbf{k}} \sum_{\mathbf{G},\mathbf{G}'} \left(\sum_i f_{i,\sigma\mathbf{k}}\phi_{i,\sigma\mathbf{k}}^*(\mathbf{G})\phi_{i,\sigma\mathbf{k}}(\mathbf{G}') \times\right.\right. \\
&\qquad\qquad \left.\left. \times \sum_s S_s(\mathbf{G}'-\mathbf{G})V_s^{NL}(\mathbf{k}+\mathbf{G},\mathbf{k}+\mathbf{G}')\right)\right] = \\
&= -i\Omega \sum_{\sigma,\mathbf{k}} w_{\mathbf{k}} \sum_{\mathbf{G},\mathbf{G}'} \left(\sum_i f_{i,\sigma\mathbf{k}}\phi_{i,\sigma\mathbf{k}}^*(\mathbf{G})\phi_{i,\sigma\mathbf{k}}(\mathbf{G}') \times\right. \\
&\qquad\qquad \left. \times (\mathbf{G}'-\mathbf{G})e^{i(\mathbf{G}'-\mathbf{G})\cdot\mathbf{R}_I}V_{s(I)}^{NL}(\mathbf{k}+\mathbf{G},\mathbf{k}+\mathbf{G}')\right) \tag{1.67}
\end{aligned}$$

which, if we use equation (1.57), we can also evaluate as

$$\begin{aligned}
\mathbf{F}_I^{NL} &= -2\sum_{\sigma,\mathbf{k}} w_{\mathbf{k}} \sum_{i,l,m} f_{i,\sigma\mathbf{k}} \, Im\left\{\left(\sum_{\mathbf{G}} \phi_{i,\sigma\mathbf{k}}(\mathbf{G})\times\right.\right. \\
&\quad \left. \times \mathbf{G}e^{i\mathbf{G}\cdot\mathbf{R}_I}Y_{lm}\left(\frac{\mathbf{k}+\mathbf{G}}{|\mathbf{k}+\mathbf{G}|}\right) F_{s(I),lm}^{KB}(\mathbf{k}+\mathbf{G})\right)^* \times \tag{1.68} \\
&\quad \left. \times \left(\sum_{\mathbf{G}'} \phi_{i,\sigma\mathbf{k}}(\mathbf{G}')e^{i\mathbf{G}'\cdot\mathbf{R}_I}Y_{lm}\left(\frac{\mathbf{k}+\mathbf{G}'}{|\mathbf{k}+\mathbf{G}'|}\right) F_{s(I),lm}^{KB}(\mathbf{k}+\mathbf{G}')\right)\right\}
\end{aligned}$$

where $Im(z)$ means the imaginary part, $z = Re(z) + i\,Im(z)$.

22

- Ion-ion interaction:

$$\mathbf{F}_I^{ion} = -\nabla_{\mathbf{R}_I} \left(\frac{1}{2} \frac{e^2}{4\pi\varepsilon_0} \sum_{\substack{J \in cell \\ K \neq J}} \frac{Z_{s(J)} Z_{s(K)}}{|\mathbf{R}_J - \mathbf{R}_K|} \right) = -\nabla_{\mathbf{R}_I} \gamma_{Ewald}. \qquad (1.69)$$

This term is evaluated by the Ewald-sum technique.

The total expression for the forces acting on ions is thus

$$\mathbf{F}_I = -i\Omega \sum_{\mathbf{G} \neq 0} \mathbf{G} e^{i\mathbf{G} \cdot \mathbf{R}_I} V_{s(I)}^{loc}(-\mathbf{G}) n(\mathbf{G}) -$$

$$- i\Omega \sum_{\sigma, \mathbf{k}} w_{\mathbf{k}} \sum_{\mathbf{G}, \mathbf{G}'} \left(\sum_i f_{i,\sigma\mathbf{k}} \phi_{i,\sigma\mathbf{k}}^*(\mathbf{G}) \phi_{i,\sigma\mathbf{k}}(\mathbf{G}') (\mathbf{G}' - \mathbf{G}) e^{i(\mathbf{G}' - \mathbf{G}) \cdot \mathbf{R}_I} \times \right.$$

$$\left. \times V_{s(I)}^{NL}(\mathbf{k} + \mathbf{G}, \mathbf{k} + \mathbf{G}') \right) - \nabla_{\mathbf{R}_I} \gamma_{Ewald} \qquad (1.70)$$

which, once the Kohn-Sham system of equations has been solved, can be evaluated with comparatively little computational effort.

Chapter 2

The basic Sn/Ge(111) surface

The semiconducting elements in Group IV of the Periodic Table, namely, silicon, germanium, and tin in its α form (grey Sn), form crystals having the diamond structure (fcc with a two-atoms basis). Each atom is hybridized sp^3 and bound to its four nearest neighbors, the bonds forming tetrahedral angles $\theta \simeq 109°28'16'' \simeq 19.47°$ ($\cos\theta = -1/3$) with each other. The unreconstructed (111) surface for such a structure is shown in Figure 2.1: it forms a 2D triangular lattice, with a basis of one atom for each surface layer. The unit cell of this lattice is also shown: its sides are equal to the distance between two adjacent first-layer atoms (3.98 Å for Ge), that is customarily taken as the unit of measure, thus it is called a 1 × 1 cell. There is one dangling bond for each such cell: each first-layer atom is bound to its three second-layer nearest neighbors, leaving the fourth sp^3 orbital, pointing outwards the surface, unsaturated.

Having that large number of dangling bonds, diamond-structured (111) surfaces show a strong tendency to reconstruct: this is usually accomplished by the promotion of "adatoms" over the surface. There are two inequivalent sets of sites where adatoms can be adsorbed: so-called T_4 sites, with the adatom standing directly on top of a second-layer atom (T stands for "top"; 4 is the number of nearest neighbors, including the second-layer atom), and H_3 sites, with the adatom standing over a "hole" in the first two layers (H stands for "hollow"; there are 3 nearest neighbors in this case), with a fourth-layer atom directly beneath. This is illustrated in Figure 2.2. Both experimental and computational evidence [34, 35, 36, 37, 38, 39] shows that T_4 sites are generally preferred.

In either the T_4 or the H_3 position, each adatom is bound to three atoms in the first surface layer. It takes, therefore, one adatom every three first-layer atoms (1/3 monolayer of coverage) to saturate all of the substrate's dangling bonds: this is sometimes called the "α phase" of the surface. Its unit cell has
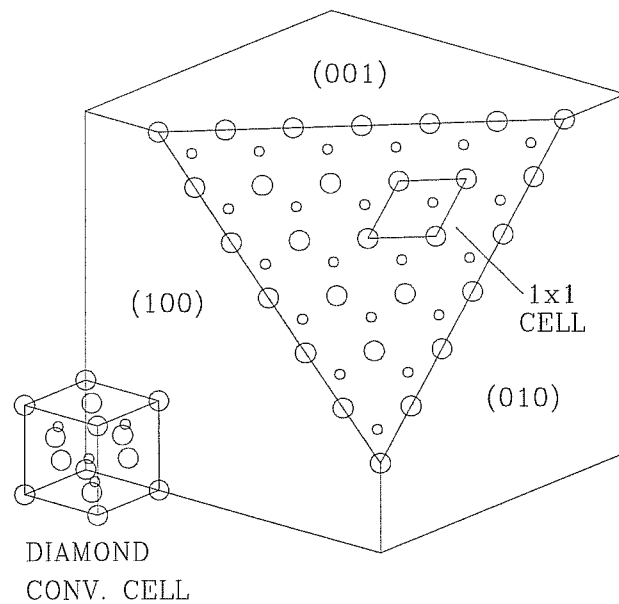
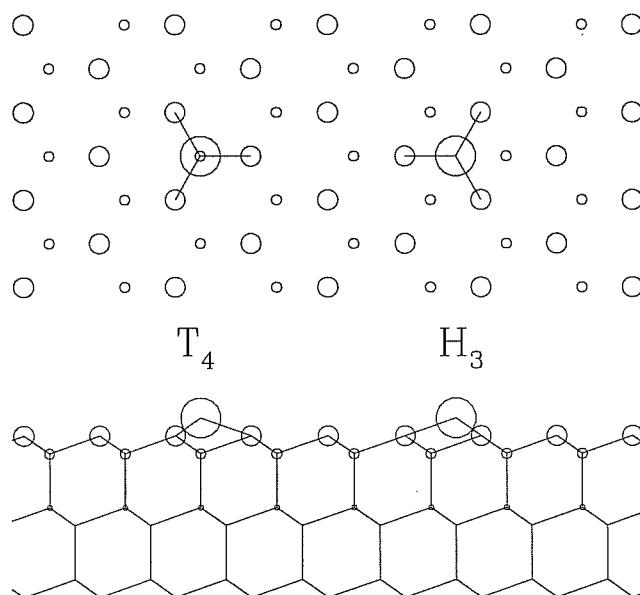Figure 2.1: The unrecostructed (111) surface of a diamond-structure crystal.

Figure 2.2: The T_4 and H_3 adsorption sites for adatoms on (111) surfaces: (a) top view; (b) side view.
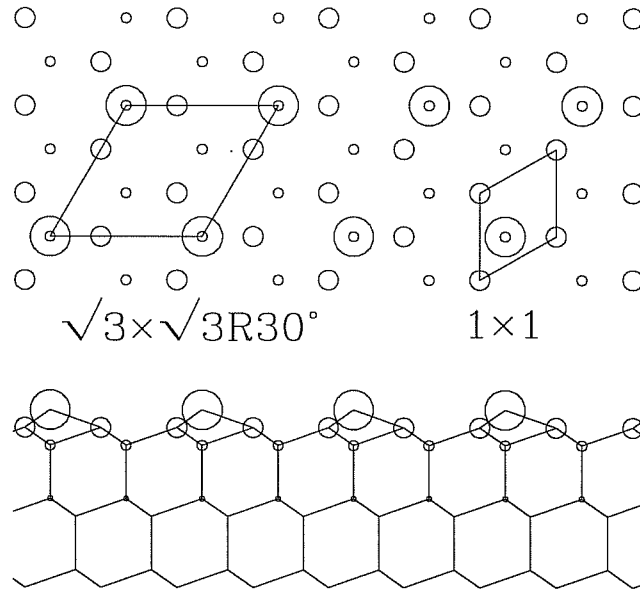
Figure 2.3: The $\sqrt{3} \times \sqrt{3}R30°\text{-}\alpha$ phase of a (111) surface: (a) top view; (b) side view.

a periodicity of $\sqrt{3} \times \sqrt{3}R30°$ (where "$R30°$" means "rotated by 30 degrees" with respect to the unrecostructed 1×1 cell), with one adatom and three atoms per layer in every cell: it is shown in Figure 2.3. This reconstruction has a threefold symmetry, being invariant under rotations of 120°.

The α phase is really very favorable when adatoms are of a trivalent species (e.g., gallium or indium): in this case, the $\sqrt{3} \times \sqrt{3}R30°\text{-}\alpha$ surface is fully passivated and insulating, and usually extremely stable.

2.1 The adatom-rest atom structure

When adatoms are tetravalent, the $\sqrt{3} \times \sqrt{3}R30°\text{-}\alpha$ reconstruction isn't so convenient as with trivalent adatoms: while all the substrate's dangling bonds are saturated, each adatom, being constrained to form three bonds, has a dangling bond originating from its unsaturated fourth orbital.

A more favourable reconstruction mechanism, effectively removing all half-filled orbitals, is provided by the formation of so-called *adatom-rest atom* (shortly A-R) pairs. The basic "A-R block" is shown in Figure 2.4: it is a 2×2 cell, containing one adatom and *four* substrate atoms per layer. The
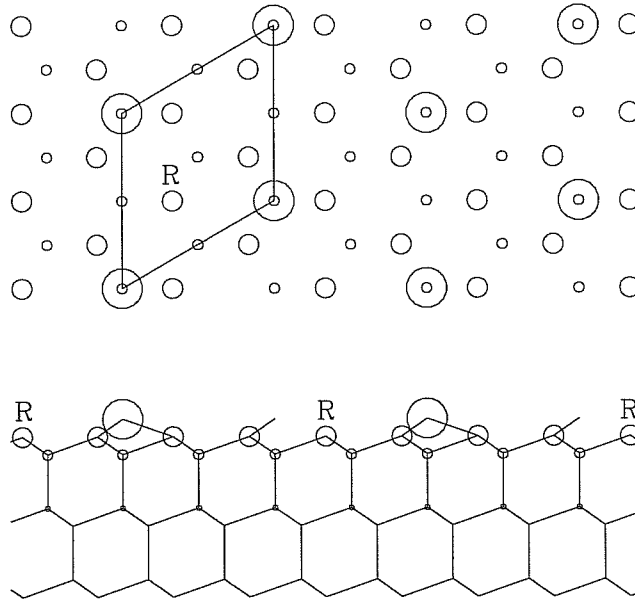
26

Figure 2.4: The basic 2 × 2 cell of an adatom-rest atom reconstruction.

adatom coverage is thus 1/4 of monolayer. Of the first-layer atoms, three are bound to the adatom, while the fourth, called the *rest atom*, is left with its dangling bond unsaturated: thus, there are two dangling bonds per cell, one on the adatom, and one on the rest atom.

This might look unfavourable at first sight; however, the adatom's and the rest atom's dangling bonds correspond to distinct surface bands at different energies, with the Fermi level pinned in between (see Figure 2.6). A charge transfer must thus occur between the two surface bands: the rest atom's dangling bond is filled by two electrons, while the adatom's one is empty. (A rearrangement of backbond orbitals also takes place, so that the true charge transfer between the two atoms is actually very much less than a whole electron.) As a consequence, in this reconstruction, both dangling bonds are passivated, and the surface becomes insulating.

The A-R mechanism appears to be a very convenient way to stabilize a (111) surface with tetravalent adsorbates: actually, clean surfaces, that is, with adatoms of the same species of the substrate, usually reconstruct following A-R based patterns. For example, the clean Si(111) surface shows the famous 7 × 7 dimer-adatom-stacking fault (DAS) reconstruction [40, 41], which is basically made up of 2 × 2 domains separated by "dimer walls", while clean Ge(111) reconstructs with a $c(2 \times 8)$ pattern [42, 43] that is also

A-R based. Theoretical calculations show that clean α-Sn(111) also follows the A-R pattern [44].

Unexpectedly, instead, surfaces with tetravalent adatoms having large atomic numbers (namely, Sn and Pb) present a stable $\sqrt{3} \times \sqrt{3}R30°$-$\alpha$ phase: this is the case, for example, with Pb/Si(111) [36, 45] (that is, Pb adatoms over a Si(111) substrate), Pb/Ge(111) [46], and with the Sn/Ge(111) surface [35, 47, 48, 49], which is the subject of this work.

2.2 Relative stability of $\sqrt{3} \times \sqrt{3}R30°$ against 2×2 phases

Based on the arguments presented above, the existence of a stable α phase in (111) surfaces with tetravalent adsorbates is rather surprising. Therefore, we carried out a computational study of the Sn/Ge(111) surface, taken as a representative case for this family of systems, to investigate the reasons for the relative stability of the α phase against the more appealing A-R reconstruction. An account of this study has been published [50].

All calculations were done using an early, scalar version of the PWSCF program (available at the URL http://www.pwscf.org/). This program solves electronic structure problems using the density functional-plane wave method with pseudopotentials (see chapter 1). We used the LDA approximation (no spin) with Becke-Perdew gradient corrections [51, 52], and a plane-wave cutoff energy of 12 Rydbergs. To sample the hexagonal Brillouin zone, we used the 3, 6, and 18 k-points sets by Cunningham [31]; when optimizing atomic positions, the single Baldereschi point [27] was used for computational efficiency.

For each surface reconstruction considered, we used a slab of 10 germanium layers (5 bilayers), with the relevant reconstruction on the top surface, hydrogen atoms saturating the bottom surface, and about 10 Å of empty space between repeated images of the slab. When optimizing atomic positions, we kept the lowest 4 Ge layers and the H layer fixed.

The computed reconstructions were the following:

- the Sn/Ge(111) $\sqrt{3} \times \sqrt{3}R30°$-$\alpha$ phase, with 3 atoms per layer in the unit cell, for a total number of 34 atoms (1 Sn adatom, 30 Ge, and 3 H). Sn adatom coverage: 1/3 ML (monolayer).

- the Sn/Ge(111) 2×2 adatom-rest atom phase, with 4 atoms per layer in the unit cell, for a total number of 45 atoms (1 Sn, 40 Ge, 4 H). Sn adatom coverage: 1/4 ML.

- the Ge/Ge(111) $\sqrt{3} \times \sqrt{3}R30°$-$\alpha$ phase, identical to the Sn/Ge(111) one, but with a Ge adatom in place of a Sn one. Sn coverage: 0.

- the Ge/Ge(111) 2×2 phase, also identical to the Sn/Ge(111) one with the adatom replaced. Sn coverage: 0.

In all of these surface relaxations, adatoms were placed in the T_4 position. In addition, we computed the minimal diamond-structure cells (2 atoms, fcc) of Ge and Sn, in order to obtain the bulk energy per atom of these substances. For these computations, we used a Chadi-Cohen 10 k-points set [28].

These four reconstructions are all possible phases of the Sn/Ge(111) surface at different Sn coverages: in particular, the Ge/Ge(111) phases can be seen as Sn/Ge(111) phases with a Sn coverage of 0 ML. The quantity that must be considered, in order to determine the stable phases of this system as a function of Sn coverage, is the thermodynamical potential (that we call "free energy" for convenience) $\Omega = E - \mu N$, where N is the number of Sn atoms, and μ is the Sn chemical potential. The number of Ge atoms, instead, is fixed, except that in the Ge/Ge(111) phases there is an extra atom, i.e., the adatom; therefore, from the energy of these phases, we subtract that of a bulk Ge atom. The chemical potential of Ge is thus fixed to the latter energy.

Stable phases of the Sn/Ge(111) surface are thus those (and only those) whose free energy is less than that of all competing phases for some value of μ. It must be noted that μ can't be greater than the energy per atom of bulk Sn: if this was the case, Sn atoms would aggregate into islands of bulk Sn, rather than being adsorbed regularly on the surface.

The computed energies (using 18 k-points) are shown in Table 2.1, and Ω is plotted as a function of μ in Figure 2.5. We obtain two stable phases, namely, the Sn/Ge $\sqrt{3} \times \sqrt{3}R30°$-$\alpha$ phase for -7.1733 Ry $< \mu < -7.1476$ Ry, and the Ge/Ge 2×2 phase for $\mu < -7.1733$ Ry. This is consistent with experimental evidence: the Sn/Ge(111) system does present a stable α phase [35, 47, 48, 49], while the clean Ge(111) surface actually reconstructs with a $c(2 \times 8)$ structure [42, 43], that we didn't consider in our computations because its unit cell was too large, but which is composed of 2×2 and $c(2 \times 4)$ blocks, both of the A-R type. We can thus expect that the energy of this phase is not very different from that of our 2×2 phase.

To explain this behavior, we examined the geometry of the optimized reconstructions. In Table 2.2, some data about the position of adatoms and rest atoms are reported: it can be seen that adatoms are pushed considerably higher than their ideal (tetrahedral geometry) position by some effect. An obvious candidate is the repulsion between the adatom and the second-layer

system	slab energy	energy/1 × 1 cell
bulk Ge (per atom)		−8.0290
bulk Sn (per atom)		−7.1476
Sn/Ge 2 × 2	−332.5274	−83.1319
Sn/Ge $\sqrt{3} \times \sqrt{3}R30°$	−251.1912	−83.7304
Ge/Ge 2 × 2	−333.3862	−81.3393
Ge/Ge $\sqrt{3} \times \sqrt{3}R30°$	−252.0442	−81.3384

Table 2.1: Energy of the calculated phases (in Rydbergs). To obtain values per 1 × 1 cell, the energy of a bulk Ge atom has been subtracted from that of Ge/Ge phases.
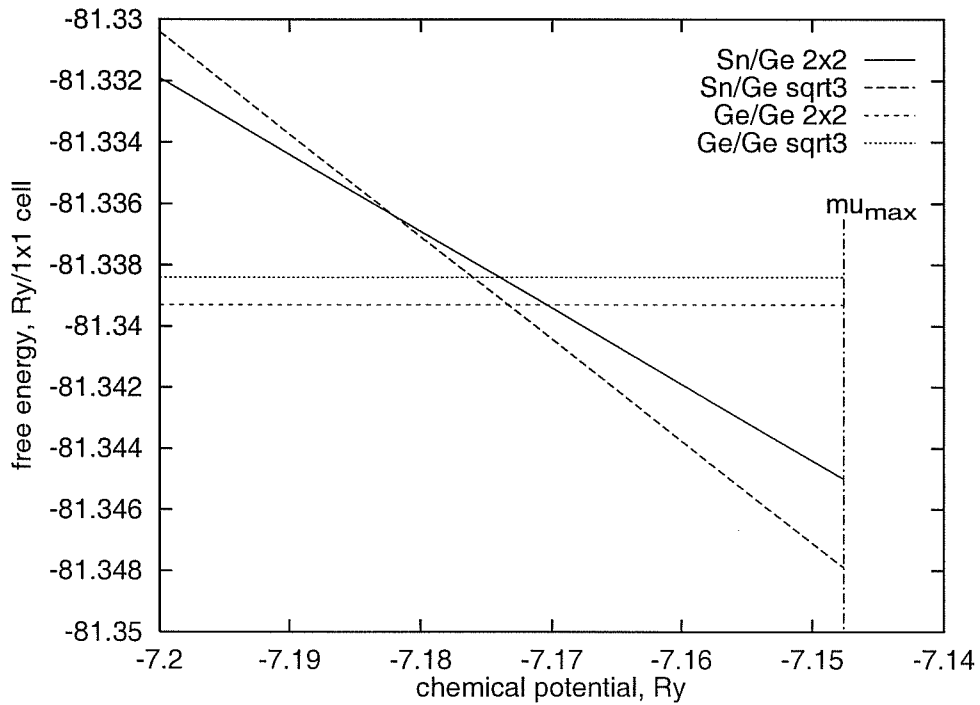
Sn/Ge 2x2 ——
Sn/Ge sqrt3 - - - -
Ge/Ge 2x2 -------
Ge/Ge sqrt3 ········

mu_{max}

free energy, Ry/1x1 cell

chemical potential, Ry

Figure 2.5: Free energy as a function of μ for different phases of the Sn/Ge(111) surface. The upper bound $\mu_{max} = -7.1476$ Ry is the energy per atom of bulk Sn.

system	bond angle	bond length	2nd-layer dist.
ideal (tetrahedral)	19.47°	2.455	1.636
Sn-Ge covalent distance	—	2.631	—
Sn/Ge 2 × 2, adatom	37.19°	2.814	2.798
Sn/Ge 2 × 2, rest atom	29.88°	2.486	—
Sn/Ge $\sqrt{3} \times \sqrt{3}R30°$	40.63°	2.816	3.042
Ge/Ge 2 × 2, adatom	33.60°	2.652	2.623
Ge/Ge 2 × 2, rest atom	30.31°	2.484	—
Ge/Ge $\sqrt{3} \times \sqrt{3}R30°$	37.90°	2.657	2.889

Table 2.2: Bond angles and lengths for adatoms and rest atoms in the computed reconstructions. All distances are in Angstroms.

atom beneath, which in the ideal geometry are far too close (only 2/3 of the Ge-Ge bond length). However there must be more than that: indeed, the optimized distance between the two atoms turns out to be much greater than the Sn-Ge bond length, at which distance repulsion should cease. Furthermore, rest atoms are also pushed up, while there's no atom directly beneath them.

We formulate the following simple argument: there is a direct relation between the geometry of sp^3 bonds formed by an atom, and its hybridization state. In particular, if we consider an adatom with its dangling bond in the vertical direction, the latter's energy is given by [53]

$$E_{db} = \varepsilon_p - \frac{9}{4}(\varepsilon_p - \varepsilon_s)\sin^2\theta \qquad (2.1)$$

where θ is the angle between the adatom's backbonds and the horizontal plane. At the tetrahedral value of $\theta \simeq 19.47°$ ($\sin\theta = 1/3$), we obtain $E_{db} = (3\varepsilon_p + \varepsilon_s)/4$, yielding perfect sp^3 hybridization; at larger values of θ, the dangling bond acquires a more s-like character, and E_{db} decreases.

Now, let us examine the electron band structure of our systems (Figure 2.6): the surface band in the middle of the gap corresponds to the adatom's dangling bond, as can be seen from Figure 2.7 (for the $\sqrt{3} \times \sqrt{3}R30°$ phase; the plot for the 2 × 2 phase is similar). In agreement with our geometrical argument, it has a lower energy for Sn/Ge than for Ge/Ge (by about 80–100 meV), both in the 2 × 2 and the $\sqrt{3} \times \sqrt{3}R30°$ phase. There is however an important difference between the two phases: in the 2×2 phase, the dangling-bond band is empty, thus lowering its energy value has little effect on the total system energy. In the $\sqrt{3} \times \sqrt{3}R30°$ phase, instead, the dangling-bond band is partially occupied, and if its energy is lowered, the total energy of

31

this phase decreases correspondingly.

This is a distinct advantage of the $\sqrt{3} \times \sqrt{3}R30°$ phase over the 2×2 phase in the Sn/Ge(111) system, and according to our results, it is sufficient to stabilize the former phase against the latter for this surface. Indeed, we can see from Table 2.2 that adatoms in the $\sqrt{3} \times \sqrt{3}R30°$ phase form larger bonding angles (by about 4°) than in the 2×2 phase: this indicates a stronger tendency to move outwards the surface, because of the greater energy gain in doing so.

The reason for Sn adatoms being higher over the surface plane than Ge ones is the larger size of Sn, which has a covalent radius of 1.40 Å, compared to 1.22 Å for Ge: bond lengths are correspondingly greater, as can be seen from Table 2.2, thus allowing adatoms to stay higher. In addition to that, a lowered dangling bond hybridizes much more strongly with states in the substrate. It has been shown [54] that the Ge-Ge bonding state directly underneath the Sn adatom is strongly involved in this stabilization procedure.

We can argue that the same mechanism also explains the stability of $\sqrt{3} \times \sqrt{3}R30°$-$\alpha$ phases on systems such as Pb/Si(111) [36, 45] and Pb/Ge(111) [46], where the adatoms are also larger than substrate atoms, while adatom-rest atom based phases prevail for equal-sized adatoms.
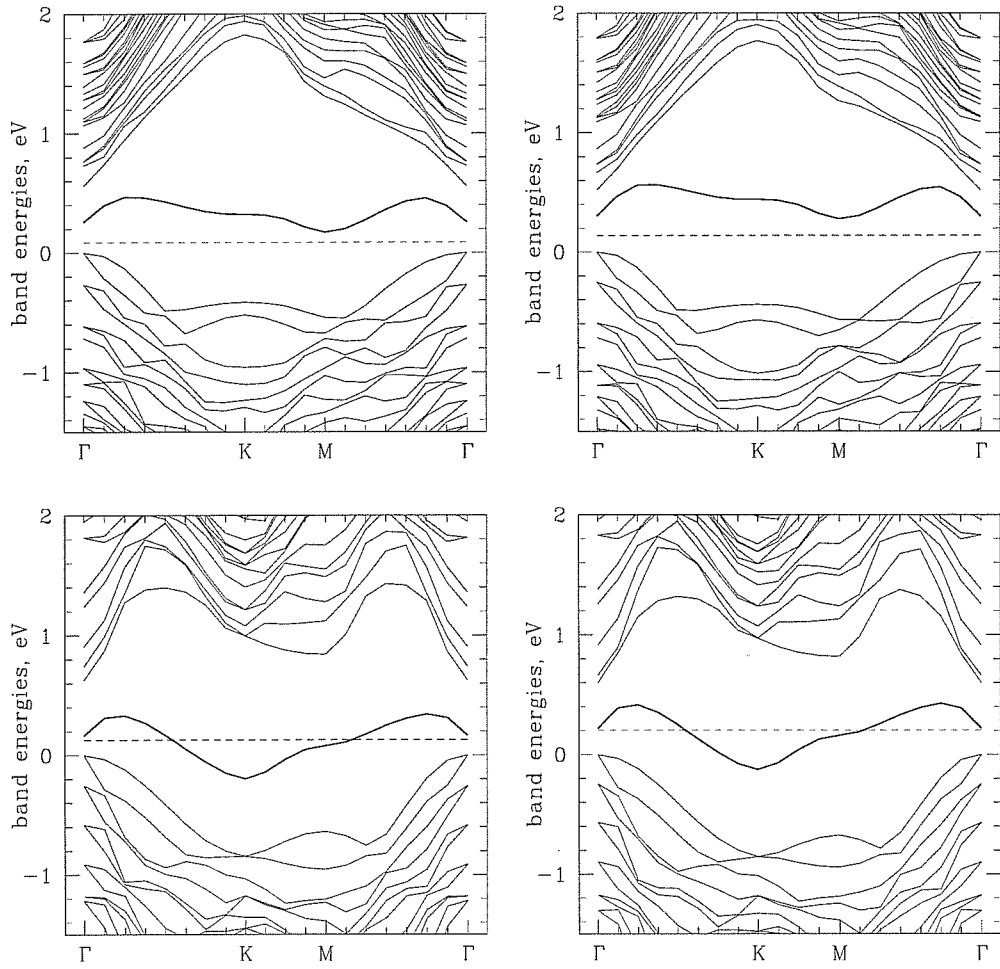
Figure 2.6: Electron bands of: (a) Sn/Ge(111) 2×2; (b) Ge/Ge(111) 2×2; (c) Sn/Ge(111) $\sqrt{3} \times \sqrt{3}R30°$; (d) Ge/Ge(111) $\sqrt{3} \times \sqrt{3}R30°$. The dashed lines indicate the Fermi energy.
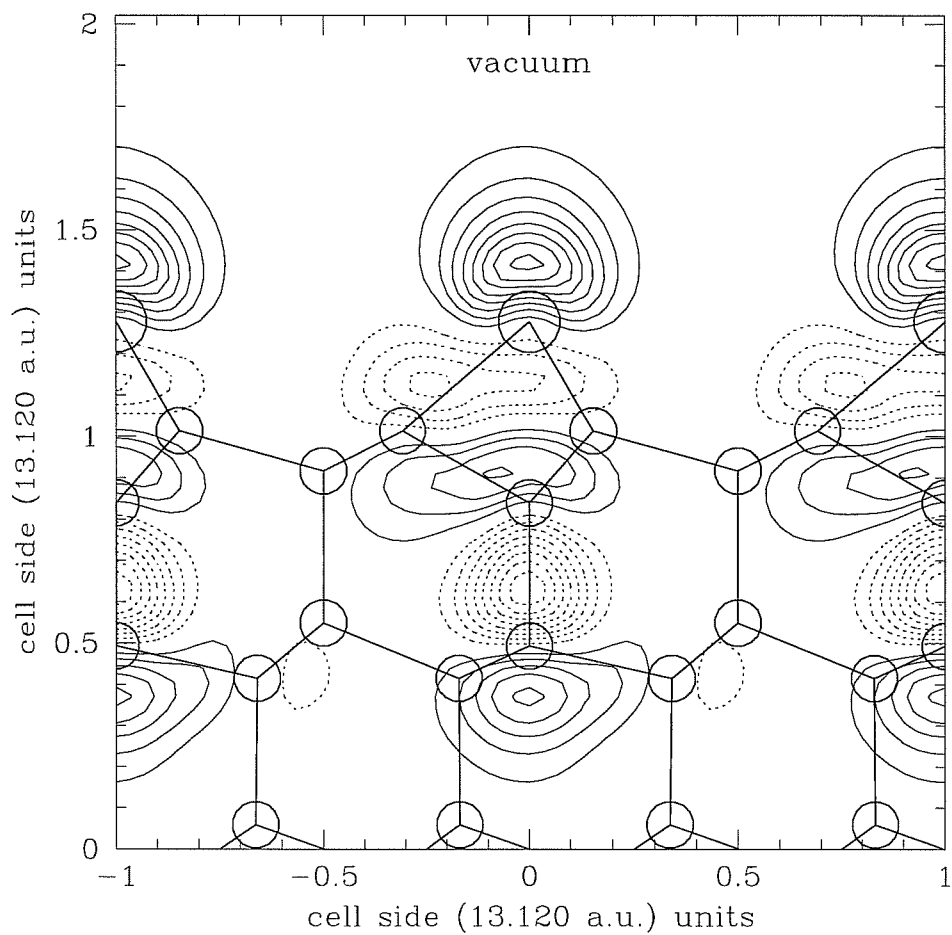
33

Figure 2.7: Contour plot of the wavefunction associated with the surface band in the middle of the gap (for the Sn/Ge $\sqrt{3} \times \sqrt{3}R30°$ phase). Solid lines: positive sign; dashed lines: negative sign.

Chapter 3

The Sn/Ge(111) 3×3 distortion

A very interesting discovery was made a few years ago by Plummer and coworkers on the Pb/Ge(111) surface [55] and later on Sn/Ge(111) [56], namely, a phase transition from a room-temperature $\sqrt{3} \times \sqrt{3}R30°$-$\alpha$ phase to a new phase with 3×3 periodicity at low temperature (for Sn/Ge, $T_c \simeq$ $-60°$C). This phase seems to be an α phase with reduced symmetry: STM images show protrusions, identified with adatoms, at the same positions as in the α phase, but while in the latter they all have the same brightness, in the 3×3 phase two sets of inequivalent adatoms appear clearly. Namely, out of three adatoms in each 3×3 cell, one is darker than the other two in STM empty-states images, thus forming a "honeycomb" pattern; in filled-states images, the situation is reversed (Figure 3.1).

Diffraction experiments on the Sn/Ge(111) surface [57, 58, 59] showed that the phase transition is accompanied by a structural distortion of the surface, extending for at least two layers into the substrate: the main feature of the distortion is a displacement of adatoms orthogonal to the surface, with the adatom appearing darker in empty-state images (from now on, the "up" adatom) higher than the other two ("down" adatoms) by about 0.3 Å over the surface plane. Similar results were found for Pb/Ge(111) [60]. We will thus refer to the room-temperature α phase as the "undistorted" phase, and to the low-temperature 3×3 as the "distorted" one; the distortion pattern will be labelled "1U", meaning "one adatom up" (and two down) per cell.

Theoretical computations [61, 62] confirmed the experimental distortion pattern, and found that the distorted phase has an energy lower than the undistorted one by an amount of order 10 meV/adatom.

Although the 3×3 distortion of Pb/ and Sn/Ge(111) has attracted considerable interest [63, 64, 65], the underlying physical mechanism is still controversial: its discoverers interpreted the distortion as a charge density wave (CDW) transition [55], but this was subsequently criticized, mainly because
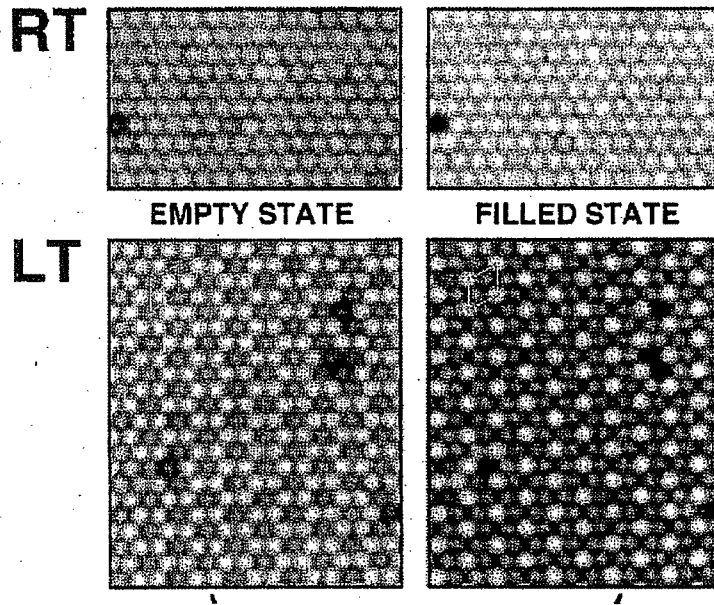
RT

EMPTY STATE · FILLED STATE

LT

Figure 3.1: STM images of the Sn/Ge(111) surface (from Ref. [56]).

of the lack of nesting [66]. Therefore, we undertook a computational study of Sn/Ge(111), in order to find a satisfactory explanation.

3.1 Basic results

All calculations were done using the parallel PWSCF program (available at the URL http://www.pwscf.org/). This program solves electronic structure problems using the density functional-plane wave method with pseudopotentials (see chapter 1). We used the LDA approximation (no spin) with and without gradient corrections (PW91 [67] and PBE [12]), and a plane-wave cutoff energy of 12 Rydbergs.

We used slabs of 6 germanium layers (3 bilayers), with the relevant reconstruction on the top surface, hydrogen atoms saturating the bottom surface, and about 10 Å of empty space between repeated images of the slab. Computations on the undistorted phase, when optimizing atomic positions, were done on a $\sqrt{3} \times \sqrt{3}$ cell: the total number of atoms in the slab was thus 22 (1 Sn adatom, 18 Ge, and 3 H). To sample the hexagonal Brillouin zone, we used Monkhorst-Pack sets [30] of 27 and 37 k-points. These large numbers are necessary in view of the metallicity of these surfaces and of the extreme

relative accuracies needed (of order 1 meV/adatom).

Once the positions have been optimized, and for all calculations on the distorted phase, we used a cell with the full 3×3 periodicity: the total number of atoms was thus 66 (3 Sn, 54 Ge, 9 H). With this cell we used sets of 12 and 16 k-points, obtained by folding the 27- and 37-points sets used with the $\sqrt{3} \times \sqrt{3}$ cell into the 3×3 irreducible Brillouin zone. Both for the $\sqrt{3} \times \sqrt{3}$ and the 3×3 slab, when optimizing atomic positions, we kept the last Ge layer and the H layer fixed.

Confirming earlier results by other researchers [61, 62], we found the 3×3 distorted phase to have lower energy than the undistorted one: using 12 (27) k-points, the energy gained by distorting is 6.5 meV/adatom in plain LDA, 9.6 meV/adatom with PW91 gradient corrections [67], and 8.7 meV/adatom with PBE gradient corrections [12]. Subsequent calculations were done using 16 (37) k-points and PBE gradient corrections; the energy gain was 8.5 meV/adatom. We refer from now on to the results of the latter calculations.

The optimized distorted and undistorted cells are shown in Figure 3.2: the distortion follows the 1U pattern. The vertical distance between up and down adatoms is about 0.34 Å, in good agreement with experimental data [58, 59]. We also tried to optimize a 2U (two adatoms up, one down) pattern, but no energy is gained by such a distortion (more on that in chapter 6).

The electron bands for the distorted and undistorted surface are shown in Figure 3.3. As a consequence of the distortion, one of the three dangling-bond bands (that coincide in part in the undistorted case) is moved down in energy, while the other two are moved up. The band splitting is of order 0.2 eV. Electron counting, and the position of the Fermi level (dashed line), show that the lower band is completely filled by two electrons, while the higher ones share a single electron, and are thus only quarter-filled.

It is therefore natural to identify the lower-energy band with the single up adatom, and the higher-energy ones with the two down adatoms: this picture correctly explains STM evidence, namely, that the up adatom, with its filled dangling bond, appears darker than down ones in empty-states STM images, while it appears brighter in filled-states images. This is also in agreement with our reasoning on adatom geometry and hybridization in chapter 2: when an adatom moves upwards, its dangling-bond band acquires a more s-like character, and thus lowers its energy. However, in doing so, it also increases its hybridization with the underlying Ge-Ge bond, so that the filled state is now only about 50% of dangling bond nature [54].
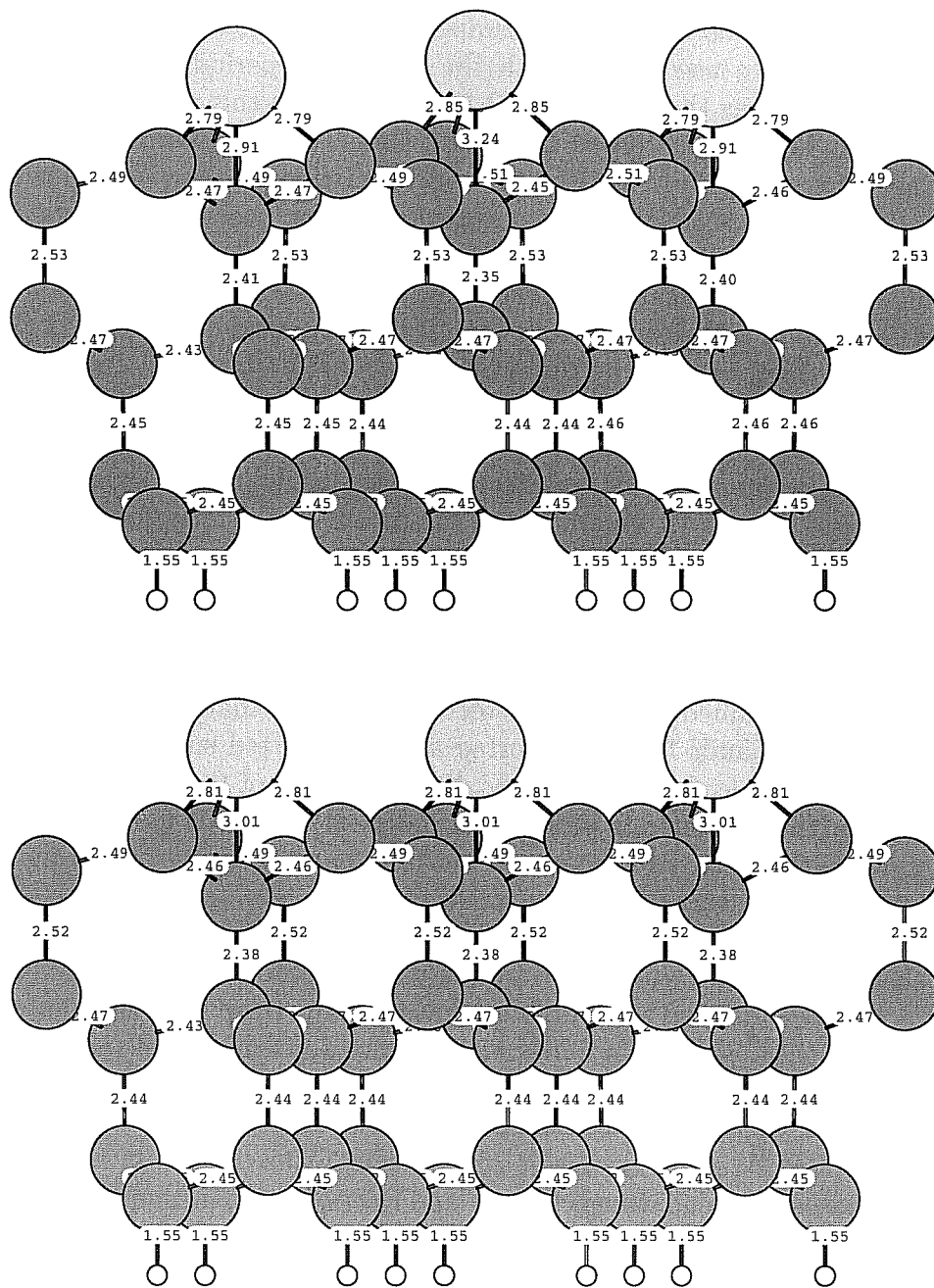
Figure 3.2: Optimized positions for: (a) the distorted cell; (b) the undistorted cell. Bond lengths are given in Angstroms.
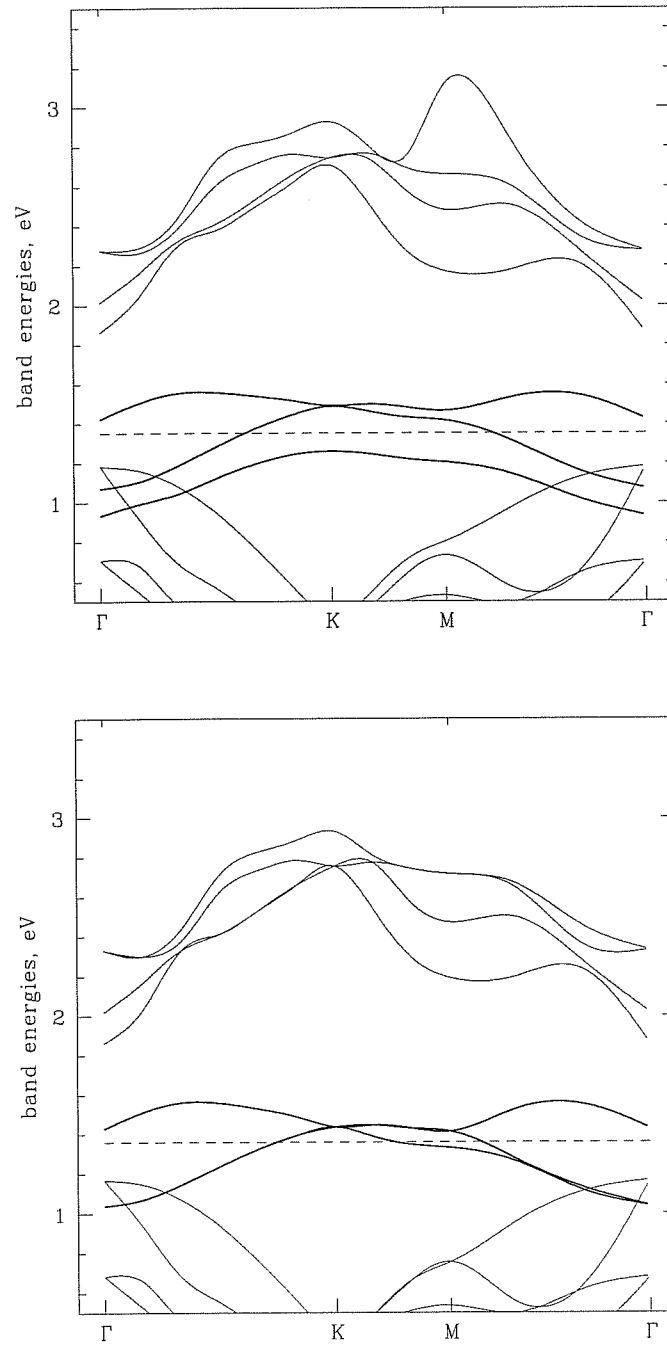
Figure 3.3: Electron bands for: (a) the distorted 3 × 3 Sn/Ge cell; (b) the undistorted one.

system	E_{kin}	E_{el}	E_{xc}	E_{tot}
3×3 distorted	164.4098	-490.2132	-137.3272	-463.1306
3×3 undistorted	164.5964	-490.3130	-137.4122	-463.1288
difference	-0.1866	$+0.0998$	$+0.0849$	-0.0019
H chain, diff.	$+0.00180$	-0.00161	-0.00081	-0.00062
polyacetylene, diff.	$+0.00471$	-0.00388	-0.00139	-0.00056

Table 3.1: Contributions to the total energy for various systems (in Rydbergs).

3.2 Analysis of the energy gain

When the $\sqrt{3} \times \sqrt{3}R30° \rightarrow 3 \times 3$ transition of Pb/ and Sn/Ge(111) was first observed by Carpinelli and collaborators [55, 56], they ascribed it to a charge density wave (CDW) driven by Fermi surface nesting. However, while that hypotesis might be appealing [68, 69], this interpretation is dubious: for example, the Fermi surface doesn't have the required nesting properties [56]. Furthermore, while the Pb/Ge 3×3 phase was characterized as semiconducting, the distorted Sn/Ge is still metallic [64, 70]. Core-level measurements also appear to be inconsistent with a CDW [70]: this is discussed in more detail in chapter 4. The true distortion mechanism is thus far from clear. Alternate explanations, such as a band Jahn-Teller effect [58] with an order-disorder transition [61, 71], have been proposed, but they are not really different from a CDW in that they invoke a one-band physics. In recognition of the important role of the substrate and of multi-band physics, a "bond-density wave" has been proposed by our group [54]. However, it is not clear how to make that idea more quantitative.

We examined the contribution of the different terms making up the total energy, i.e., the kinetic, electrostatic, and exchange-correlation energy (expressions in section 1.3), as resulting from our calculations. Results are shown in Table 3.1: the energy gain associated with the distortion comes entirely from a large decrease of the kinetic energy, which overcompensates a large *increase* of both the electrostatic and exchange-correlation energy.

To determine by comparison the expected behavior for a single-band mechanism like a CDW or a Jahn-Teller distortion, we examined a couple of simple models. The first was a linear chain of hydrogen atoms, that we considered in two different configurations: in the "undistorted" one, all neighboring atoms are at the same distance (which we set to the computed optimized value, $d = 1.010$ Å), while in the "distorted" phase, dimers are formed by displacing every two consecutive atoms in opposite directions along
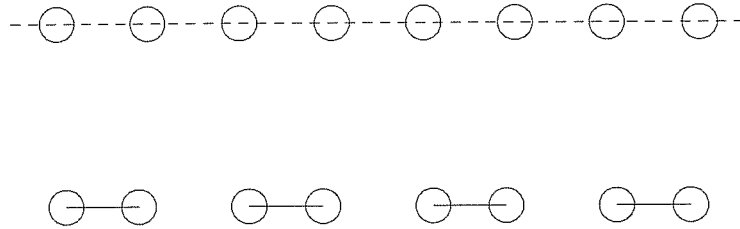
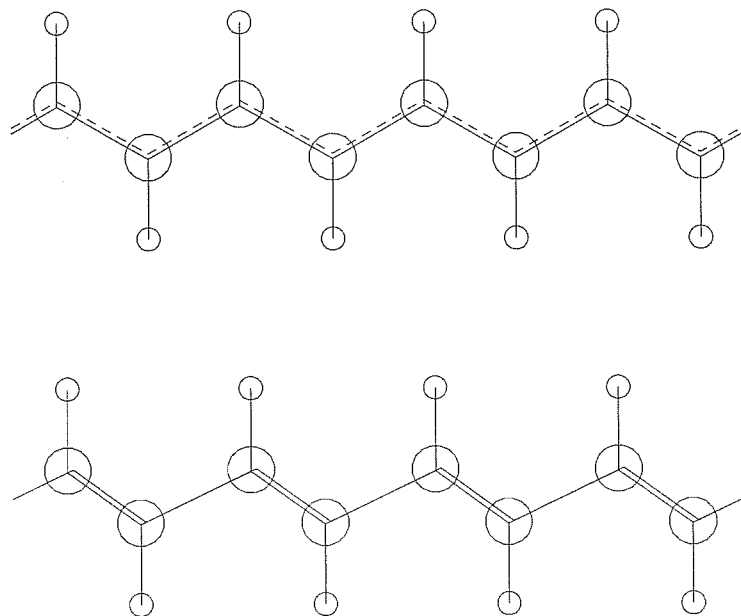Figure 3.4: (a) the "undistorted" hydrogen chain; (b) the "distorted" one.

Figure 3.5: (a) the "undistorted" polyacetylene chain; (b) the "distorted" one.

the chain, by 1% of their distance (Figure 3.4). The second model was an infinite polyacetylene chain, that we "dimerized" in a similar way by alternating longer and shorter ($d = 1.424$ Å $\pm$ 1.25%) C—C bonds (Figure 3.5).

Results for these "toy systems" are also reported in Table 3.1. We can see that they both show the opposite behavior to that of the Sn/Ge system, namely, the kinetic energy increases while the potential terms (electrostatic and exchange-correlation) decrease. This behavior can be understood by noticing that a CDW, or a band Jahn-Teller effect, are nothing else than a weak attempt at forming a molecular bond. As shown, e.g., by Slater [72], modifying the molecular bond length in H_2 costs kinetic energy and gains potential energy. The kinetic energy cost in particular is due to electron localization in the shorter bond.

These data clearly suggest that the 3 × 3 distortion of the Sn/Ge(111) surface can't be simply identified as a CDW, nor as a band Jahn-Teller distortion. Again, they suggest that the distortion mechanism can't be adequately described as a single-band effect: as also suggested by our reasoning in chapter 2, the hybridization state of adatoms must be considered. More evidence, pointing in the same direction, is collected in the next chapters.

Chapter 4

Sn/Ge(111) core levels and work function

4.1 Core levels

The first piece of experimental evidence indicating the existence of two inequivalent sets of adatoms on the Sn/Ge(111) surface was observed some time before the discovery of the 3×3 distortion (and remained unexplained up to then). It came from core-level measurements: the observed photoemission spectrum for the $4d$ level of Sn adatoms below T_c is clearly split into two components, separated by about 0.32 eV [49, 70, 71] (Figure 4.1). The component with lower kinetic energy, corresponding to the deeper of the two core levels, is about half as intense as the other one: it is therefore natural to identify them with "up" and "down" adatoms, respectively, since there are twice as many of the latter as of the former in the 1U reconstruction pattern.

A rather surprising fact is that the same spectrum is observed at room temperature, that is, well above T_c, where the system is in the nominally undistorted phase [70, 71]. This suggests that the $\sqrt{3} \times \sqrt{3}R30° \to 3 \times 3$ transition is of strong order-disorder type: the surface is always instantaneously and locally in the 3×3 phase, but at room temperature, it fluctuates very rapidly, every adatom jumping up and down, so that a "slow" technique like STM can only observe an average of the three possible orientations. Thus all adatoms appear equivalent in STM. At low temperature, instead, fluctuations are frozen out, and a static 3×3 pattern can be observed.

The identification of the deeper component of the Sn $4d$ spectrum with up adatoms, and of the shallower component with down ones, is however not guaranteed. Indeed, one might even expect the contrary: namely, since the up adatom has one extra electron in its surface band (while down ones
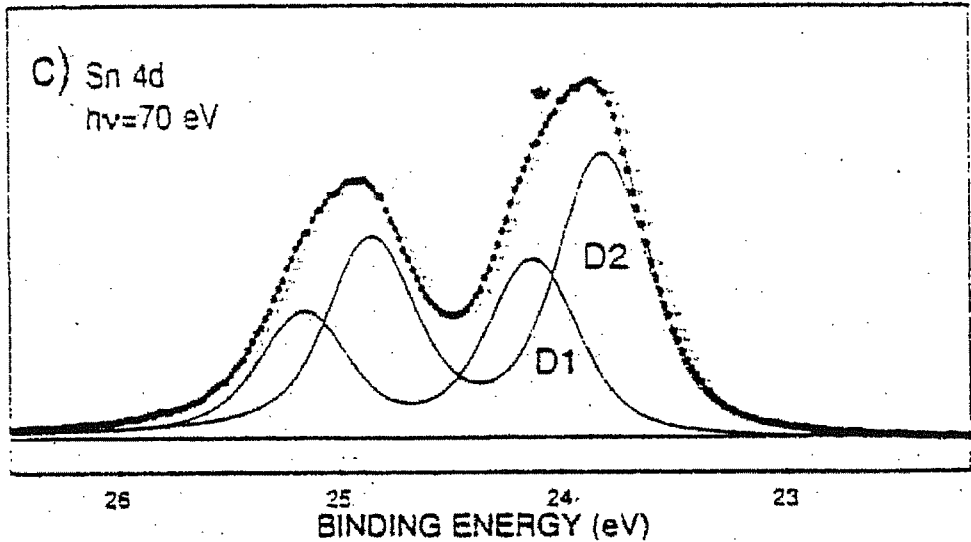
Figure 4.1: Photoemission spectrum of the $4d$ Sn core level (from Ref. [49]).

have one half electron less), the core electron in the up adatom could feel the electrostatic repulsion exerted by the extra electron. Thus its energy would be increased, making it correspond to the higher-energy component, rather than to the lower-energy one. If this were the case, the distortion pattern revealed by the core spectrum would actually be 2U. In particular, this is definitely what one should expect if the distortion were a charge density wave, that is, if a true charge transfer occurred between up and down adatoms.

We undertook a theoretical calculation of the core level splitting in the Sn/Ge(111) 3 × 3 phase. To our knowledge, no such calculation has been reported yet. The computational machinery was the same as in chapter 3: we used the same 3 × 3, 6-layers slab, with 16 k-points and PBE gradient corrections [12]. Atomic positions were kept fixed to the optimized positions computed for the 3 × 3 distorted phase (with the 1U pattern).

We computed the core-level splitting using the Pehlke-Scheffler final-state method [73]: a norm-conserving pseudopotential was generated for the excited Sn ion with an electron extracted from the $4d$ level (that is, the Sn atom just *after* photoemission), and this was used in place of the neutral-Sn pseudopotential for one of the adatoms. We did two separate runs, using the "excited Sn" pseudopotential either for the up adatom, or for a down one: the difference in the total energy between the two runs yields directly the splitting between the two core levels. We obtained a splitting of 0.202 eV, compared with the experimental value of 0.32 eV [49]; the deeper of the two

44

levels resulted that of the up adatom, contrary to the electrostatic repulsion argument, and in agreement with the 1U model.

We explain this splitting as follows: as can be seen from the plot of electron bands (Figure 3.x), the dangling bond band of the up adatom is about 0.2 eV less than that of down adatoms (0.229 eV at the K point), which in turn pins the Fermi level. If no charge transfer actually occurred between up and down adatoms, all of the adatoms' levels would be also rigidly shifted by the same amount, giving rise to a core level splitting nearly the same magnitude of the computed one. We conclude that the effect of electrostatic repulsion is rather small, which in turn implies that the excess of charge in the up adatoms is also small. Therefore, the extra electron in the up adatom's dangling bond band must come from the other orbitals of the same atom (i.e., the backbonds), through a substantial rehybridization: that is, the charge transfer is *intra*-adatom, rather than *inter*-adatom.

4.2   Work function

A second piece of evidence revealing the presence, or the absence, of an inter-atomic charge transfer, might come from the work function: if up adatoms, in the 3×3 distorted surface, were actually negatively charged, and down adatoms positively charged, a strong dipole would form at the surface. As a consequence, the work function of the distorted surface would be considerably higher than that of the undistorted one, where that dipole is absent.

To test this prediction, we computed the work function of the distorted and of the undistorted surface. We used the same computational methods as for the core levels; to determine the work function, we plotted the Hartree potential averaged on planes parallel to the surface, as a function of the orthogonal coordinate. The potential was shifted so as to set the Fermi level to zero. This is expected to be constant in the vacuum layer separating the two slabs (a thicker vacuum layer was used to enhance this effect); this constant value is thus exactly the value of the work function.

However, our slabs have two different surfaces, namely, the 3×3 distorted or undistorted Sn/Ge(111) on one side, and the H-saturated, unreconstructed Ge(111) surface on the other side. Since the two surfaces have different work functions, the Hartree potential in the vacuum, rather than being constant, turns into a straight line with a nonzero slope, smoothly joining the two surfaces (Figure 4.2). This implies that a constant electric field is present in the vacuum region: the two surfaces act as the plates of a capacitor, with opposite charges on them.

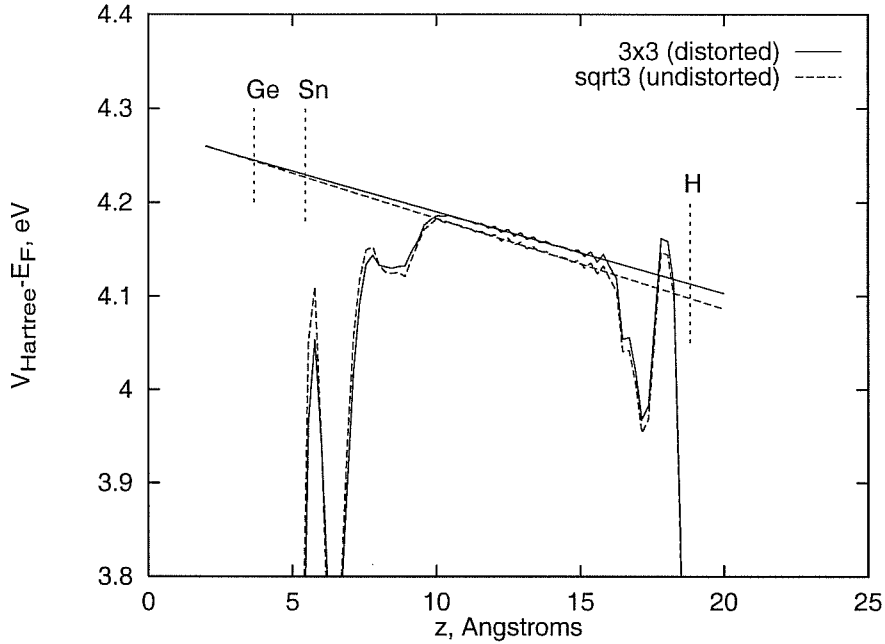To extract the value of the work function, we fitted the potential to a

Figure 4.2: Hartree potential, averaged on planes parallel to the surface, as a function of the orthogonal coordinate. The zero is set at the Fermi energy.

linear function in the vacuum region; then, we took the extrapolated value of that function at the surface edge. The main source of uncertainty is the position of the surface edge: we chose the average height of Sn adatoms, obtaining a work function of about 4.23 eV for both the distorted and the undistorted surface. This compares fairly well with an experimental value of 4.43 eV [74]. By choosing instead the average height of the first Ge layer as the surface edge, we obtained a value ~20 meV higher. This uncertainty is however canceled out when computing the difference between the distorted and undistorted work functions: it turns out to be less than 3 meV (at the Sn height $\phi_{dist} = 4.230$ eV, $\phi_{undist} = 4.227$ eV).

The near coincidence of the two work functions is thus an additional argument in favour of the inexistence of an interatomic charge transfer: this rules out the possibility that a single-band mechanism, such as CDW or Jahn-Teller, might explain the distortion. A satisfactory explanation for the distortion must therefore take into account the rehybridization of the adatoms' orbitals, that accompany the transition.

46

Chapter 5

Magnetic phases in Sn/Ge(111)

The interpretation of the 3 × 3 distortion of Pb/Ge(111) and Sn/Ge(111) as a charge density wave has been criticized mainly because of the lack of Fermi surface nesting [66]. However, that aspect may change in presence of a finite magnetization. Our group in fact showed [65] that for the Si/Si(111) surface, taken as a test case, while the LDA non-magnetic state fails to show good nesting properties, a very strong, nearly perfect electron-hole nesting is obtained for a phase with a total net magnetization of $(1/3)\mu_B$ per adatom. For that surface, in fact, the ground state was eventually shown to be a magnetic 3 × 3 with a sizeable exchange splitting suggesting closeness to an insulating state. That at first appeared to link well with the properties of the Pb/Ge(111) surface, then believed to be insulating, with a small gap of about 65 meV [55].

Moreover, other isoelectronic surface systems exhibit even stronger insulating character, in spite of their apparently odd electron number per cell. For example, the Si/SiC(0001) $\sqrt{3} \times \sqrt{3}R30°$ surface has a gap as large as 2.0 eV, explained by characterizing the system as a Mott-Hubbard insulator [75]. It was known that in a surface system of that kind, whose physics is driven by a narrow exactly half-filled surface band (the bandwidth for Si/SiC(0001) is 0.35 eV; that of Sn/Ge(111) is about 0.6 eV), an antiferromagnetic, insulating ground state can well be expected [66].

Motivated by these facts, we performed a computational study of the Sn/Ge(111) 3 × 3 surface, specifically looking for magnetic phases. The computational machinery was the same as in chapter 3, except that the local-*spin*-density approximation was used, i.e., we allowed for the system to develop a spin polarization. We used PBE gradient corrections [12], and our 12 k-points set. Starting from the optimized 3 × 3 distorted configuration, no magnetization spontaneously showed up. Even if we start with a finite initial spin polarization, the final electronic state evolved self-consistently to

47

a non-magnetic state.

To explore further that route, we used the following standard method to force a magnetic state. We kept the magnetization at a fixed value, by considering two separate spin-up and spin-down Fermi levels and assigning occupation numbers to spin-up and spin-down wavefunctions independently, according to the sum rules

$$\sum_{i,\mathbf{k}} w_{\mathbf{k}} f_{i,+\mathbf{k}} = \frac{1}{2}(N_e + \Delta N_e) \qquad \sum_{i,\mathbf{k}} w_{\mathbf{k}} f_{i,-\mathbf{k}} = \frac{1}{2}(N_e - \Delta N_e) \qquad (5.1)$$

where N_e is the number of electrons per cell, and we set $\Delta N_e = 1$. The system was thus artificially constrained to have one spin-up electron in excess, i.e., a magnetization $M = 1$ μ_B/cell.

Of course two separate Fermi levels are unphysical, but that is just another way of mimicking a strong uniform external magnetic field B such that its Zeeman splitting $2\mu_B B$ coincides with the Fermi level splitting, spin-up and spin-down bands shifted in opposite directions by $\mu_B B$. The equivalence is set by $B = (E_{F-} - E_{F+})/2\mu_B$. Since the exact dependence of the magnetization M on the field B is not known, we cannot determine a priori the right value of B for a given M. Our method allows us to specify the target value of M, effectively adjusting B so as to fit it.

We followed this procedure: first we relaxed the atomic positions (keeping the lowest Ge layer and hydrogens fixed, as usual) while keeping the magnetization fixed. The state so obtained exhibits a marginal energy gain (about 0.3 meV/adatom) over the non-magnetic, undistorted state. The difference between the two Fermi levels was about 29 meV, yielding an external magnetic field $B = 0.0011$ atomic units (about 250 T). Then, after optimizing the atomic positions, we removed the constraint on the magnetization, resorting back to a single Fermi level (i.e., $B = 0$), and relaxed the positions again.

We obtained in this way a locally stable magnetic and structurally distorted phase with 3 × 3 periodicity, with a total magnetization of about 0.17 μ_B/cell (0.06 μ_B/adatom) with an energy gain of 3.4 meV/adatom over the non-magnetic undistorted phase. This is however still 5.3 meV/adatom higher than the 3 × 3 non-magnetic distorted phase, meaning that the latter is still the ground state of the Sn/Ge(111) system, while the magnetic phase is metastable.

The main structural feature of this magnetic-distorted phase is that the three adatoms in the unit cell are all inequivalent, placing themselves at different heights; the underlying 2nd-3rd layer bond is also modulated correspondingly. Taking the height of the "middle" adatom as zero, the other two are 0.14 Å above and 0.13 Å below, respectively.
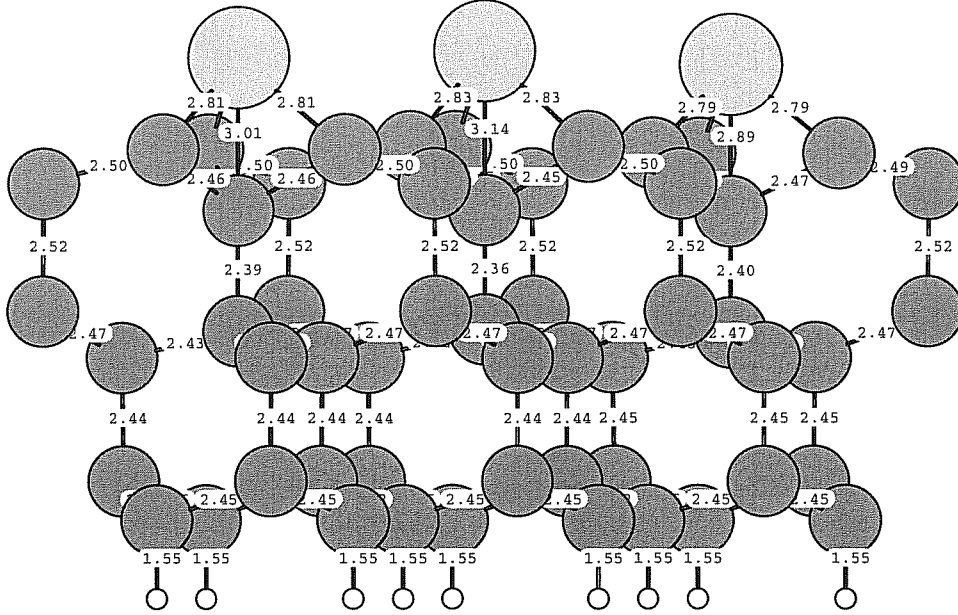
Figure 5.1: Atomic positions for the 3 × 3 magnetic-distorted state.

The electronic bands for this phase, and for the phase with $M = 1$ μ_B/cell (where the atomic positions are very similar), are also shown in Figure 5.2. It can be seen that in both phases, the system is still metallic. The exchange splitting is present, and large. The metallicity arises due to band overlap.

Because the energy differences obtained in this manner are marginal with respect to our relative accuracy, it seems important to repeat these calculations with increasing k-point sampling. Repeating the calculation using an improved 16 k-points set (see chapter 3), we obtained a very similar energy gain of 3.3 meV/adatom, 5.2 meV/adatom higher than the non-magnetic ground state. The atomic positions were also very similar to those obtained with 12 k-points. However, the total magnetization was somewhat higher, namely $M = 0.31$ μ_B/cell (0.10 μ_B/adatom). That might be due to the fact that the 16 k-points set contains the M point $(2\pi/a)(1/2, 1/2\sqrt{3})^T$, while the 12 k-points set doesn't.

Finally, we repeated again the calculation using an even larger, 36 k-points set. This time, when optimizing atomic positions, the system spontaneously evolved towards the non-magnetic, 3 × 3 distorted ground state. This means that the magnetic-distorted state found with 12 and 16 k-points lies actually in a very flat region, so that the optimization algorithm stops, but may not
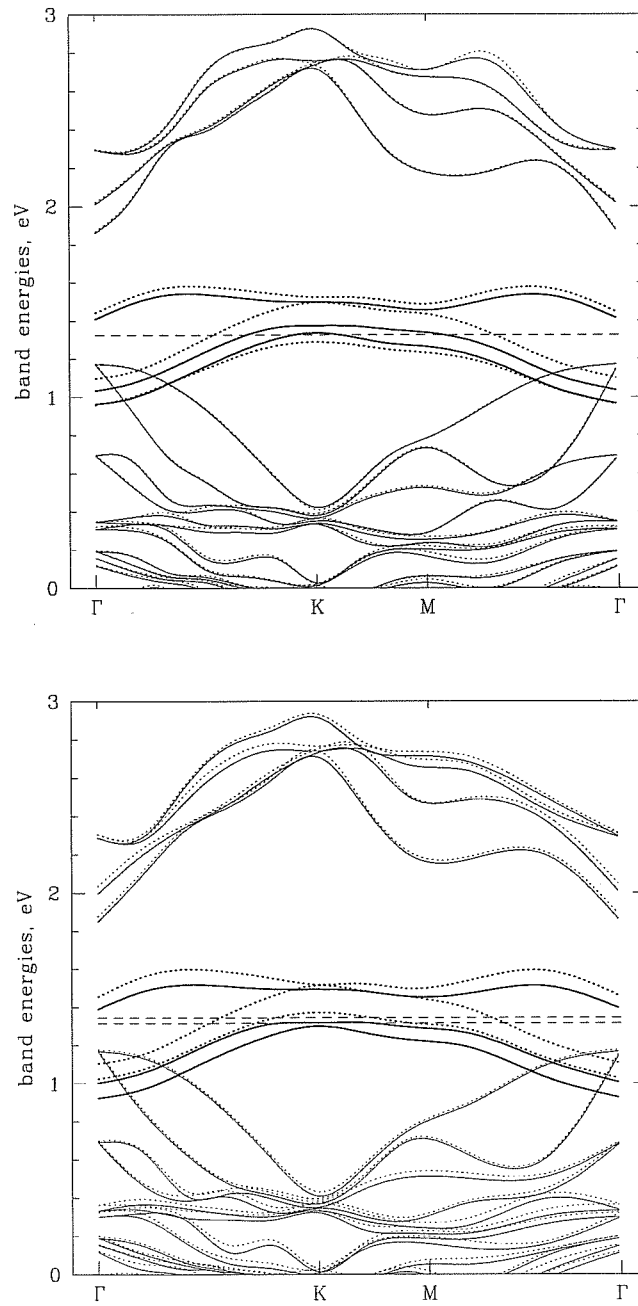
49

Figure 5.2: Electron bands of: (a) the 3×3 magnetic-distorted state; (b) the state with $M = 1 \ \mu_B$/cell. Solid lines: spin-up bands; dotted lines: spin-down bands. The dashed lines indicate the Fermi levels (two in (b)).

represent a true local minimum. It is also possible that a very small energy barrier appears as an artifact of the calculation with small k-points sets, while it disappears with a larger set.

Anyway, contrary to our expectations for narrow-band systems, no clear insulating ground state is found. Our magnetic-distorted solution is at best a local minimum, and furthermore it exhibits a weak metallic character due to band overlap. While that might well be an artifact due to the LDA gap problem, we believe that the prevalence of the non-magnetic periodically distorted state in 3 × 3 Sn/Ge(111) is likely, although with a very large density of states at E_F, and thus a large magnetic susceptibility.

The next question is: why does a Mott-Hubbard (magnetic) insulator prevail in the Si/SiC(0001) surface, and on the contrary a non-magnetic lattice distorted state in Sn/Ge(111)?

We attribute that to the fact that unlike the former, the latter surface cannot at all described by single-band physics. That in turn can be traced to a strong hybridization between the adatoms dangling bonds and some electronic states in the Ge substrate, in particular with the 2nd-3rd layer bond directly under each adatom (see Refs. [50, 54]). Because of the large band gap, small relaxations and stiffer bonds make that hybridization much smaller in Si/SiC(0001), which remains effectively single-band, than in Sn/Ge(111), which does not. Even the strong Fermi surface nesting exhibited by the Si/Si(111) magnetic phase [65], a clear precursor signal of the Mott-Hubbard state, cannot be reproduced for Sn/Ge(111) (not even with $M = 1$ μ_B/cell).

In summary, our results indicate that, at least for Sn/Ge(111), weak magnetism is not excluded (in particular the calculated susceptibility is very high) but should be regarded at most as a secondary effect.

Chapter 6

Sn/Ge(111) under strain

Any given, locally stable state of a surface, of free energy f, is characterized by its surface stress tensor, $\sigma_{ij} = -\partial f / \partial \varepsilon_{ij}$, where ε_{ij} is the strain tensor. Therefore, two given reconstructions, which in the absence of strain may be in a certain order, say $f_1 < f_2$ (f_1 stable, f_2 metastable), may reverse under a suitable strain, since $f_2 - f_1 = \int d\varepsilon_{ij}\sigma_{ji}$ may change sign.

In this picture, the 3×3 distortion of Sn/Ge(111) can itself be seen as a way to lower the surface free energy relative to the undistorted surface. If we artificially expand or compress the surface, we could modify this state of affairs, and at some critical value of strain, the distortion might disappear.

Therefore, we conducted a systematical study of the Sn/Ge(111) 3×3 phase under strain. All calculations were done using the same methods of chapter 3; since however we had to perform a very large number of runs, we used a Monkhorst-Pack 6 k-points set [29, 30] to reduce the computational cost. We strained the Sn/Ge(111) 3×3 system isotropically in the surface plane, by changing the cell side by amounts ranging from -5% to $+4\%$. The slab could freely adjust its thickness in the orthogonal direction and we allowed the atomic positions (except the bottom Ge layer and the saturating hydrogens) to relax.

For each value of the strain, we sistematically computed the energy change $E_{dist} - E_{und}$ as a function of the "distortion" (the difference in height between up and down adatoms), kept fixed while atomic positions were allowed to relax; the results are plotted in Figure 6.1. For a strain between $+2\%$ and -4% (positive strain = expansion; negative strain = compression), the energy gain showed indeed a decrease roughly linear with the strain; at the expansion of 4%, the 1U distortion practically disappears.

One could at this point surmise a simple picture: the 1U distortion is forced by an effective compressive stress, causing one adatom out of three to "pop up"; when the surface is allowed to expand, the popping ceases,
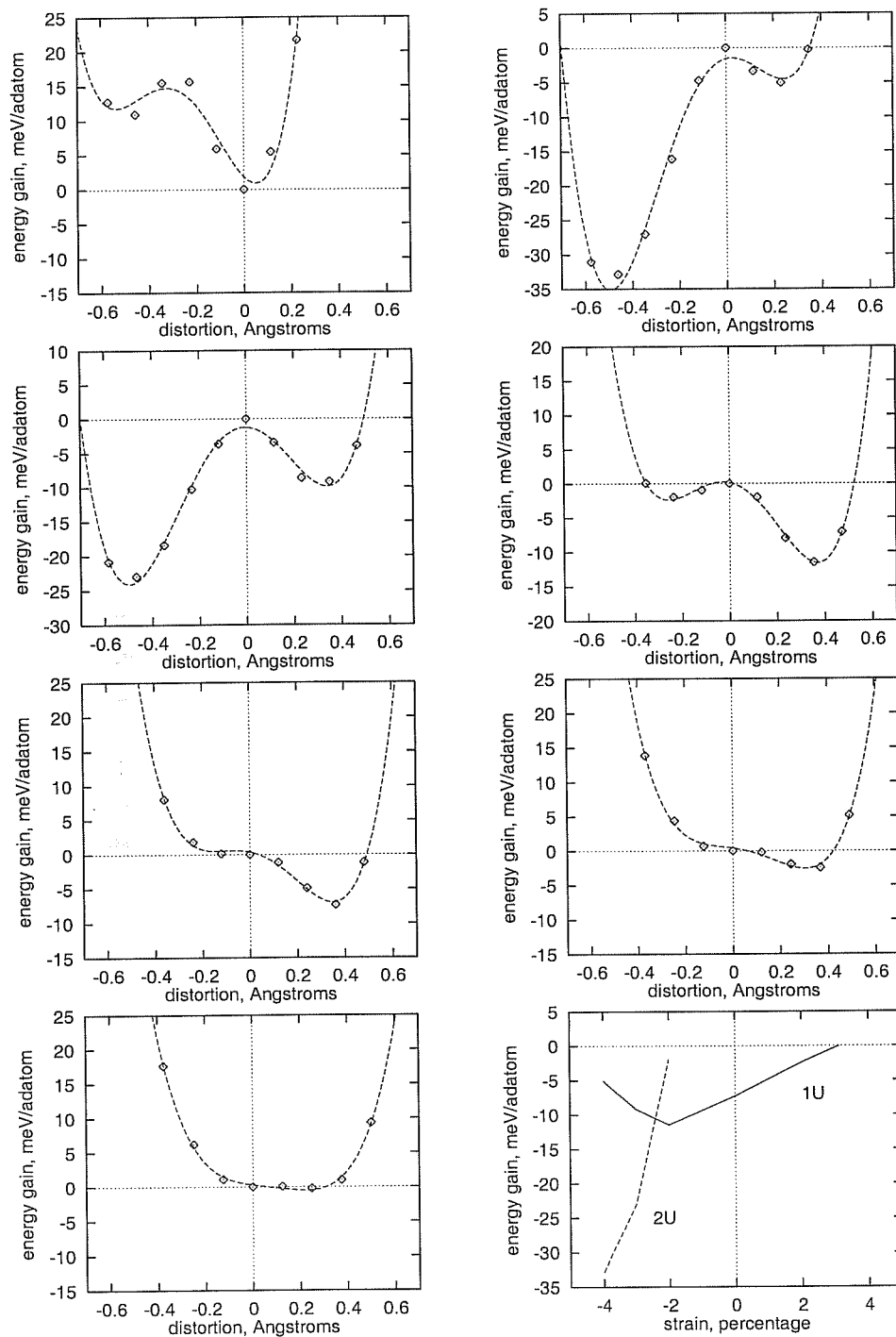
Figure 6.1: Energy gain as a function of the height difference $z_U - z_D$, for different values of strain: (a) -5%; (b) -4%; (c) -3%; (d) -2%; (e) 0; (f) $+2\%$; (g) $+4\%$; (h) optimal energy gain as a function of strain.

strain	pattern	Δz_{UD}	Δz_{U1}	Δz_{U2}	Δz_{D1}	Δz_{D2}
−5%	3U	—	1.998	3.396	—	—
−4%	2U	0.483	1.983	3.341	1.716	2.875
−3%	2U	0.473	1.972	3.313	1.714	2.865
−2%	1U	0.353	1.960	3.279	1.766	2.940
0	1U	0.344	1.940	3.235	1.753	2.912
+2%	1U	0.337	1.918	3.202	1.742	2.890
+4%	0U	—	—	—	1.774	2.947

Table 6.1: Vertical distances between adatoms and their nearest neighbors for different values of strain. U = up adatoms; D = down adatoms; 1 = first-layer atoms; 2 = second-layer atoms. All distances are in Angstroms.

and there is no more distortion. However, that is too simple: in fact, when we proceeded to calculate the intrinsic surface stress of Sn/Ge(111) at zero strain, we found it compressive, i.e., with the wrong sign. We measured it by registering the minute, but unmistakeable change of the in-plane equilibrium lattice constant of the Ge(111) slab, from −0.16% with both surfaces H-saturated, to −0.84% with one surface H-saturated and the other with 1/3 ML Sn coverage.

Hence, the Sn/Ge(111) surface wants to contract, not to expand; then why does one adatom out of three want to pop up? Indeed, the overall picture seems to be more complex. When compressing by 3% and 4%, we found a new and surprising result: a deep minimum appears in the energy plot for a *negative* distortion, meaning a ground-state configuration with *two* adatoms up out of three (2U). The usual configuration, with one adatom up out of three, is instead 1U. [We note that a 2U pattern has been recently observed [76] on a patch of the Sn/Ge(111) surface.] Moreover, by increasing further the compression to 5%, the situation changes again, the undistorted phase becoming again the ground state.

The vertical distances between adatoms and their first- and second-layer nearest neighbors are reported in Table 6.1 and plotted in Figure 6.2. Strikingly, these vertical distances hardly change with strain. Every adatom is either up (U) or down (D), and never in between. For zero strain U = 1, D = 2; but at 3% compression U = 2, D = 1, and at 5% compression U = 3, D = 0. We label the latter (undistorted) phase "3U". Conversely, by expanding of 4% we find U = 0, D = 3: this state is again undistorted, but now "0U". Compression actually favours the distortion, but instead of the expected "continuous" effect, we get a "discrete" one: at intervals, an adatom jumps suddenly from the lower site to the upper one.
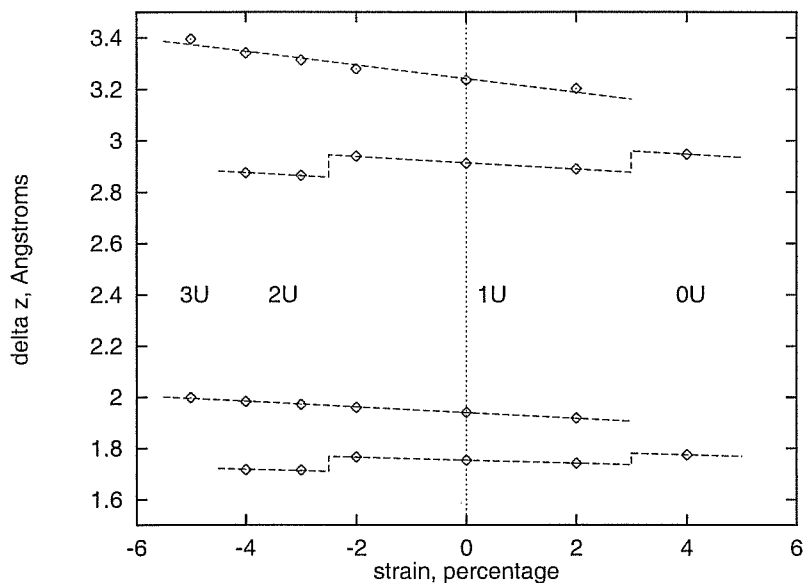
Figure 6.2: Vertical distances as a function of strain (see Table 6.1). From top to bottom: Δz_{U2}, Δz_{D2}, Δz_{U1}, Δz_{D1}. The steplike increases of Δz_{D1} and Δz_{D2} appear in correspondence with transitions between different patterns.

It is interesting to observe that for the similar Sn/Si(111) surface, while a 3×3 distortion has been looked for without success, core-level measurements show a splitting of the Sn $4d$ level, just as for Sn/Ge(111) (except that relative intensities suggest a 2U pattern instead of 1U) [77]. We may argue that at zero strain, the Sn/Si(111) surface is either in a 0U or 3U phase, but that at some values of strain, a distortion might show up. G. Profeta [78] is currently investigating this possibility.

6.1 Mixed valence on Sn/Ge(111)?

The results above are possibly the most important in this thesis. Because they were discovered only near the end, they are to a large extent still under scrutiny. Here are a few considerations and tentative points that we aim at pursuing as early as possible.

Application of surface strain has uncovered two main facts. First, each Sn adatom has basically two positions, U and D, and there is presumably an energy barrier in between. Second, the relative abundance U/(U+D) can be changed from 0 to 1/3, 2/3, and 1 by compression. Mechanically, this is clear enough, since in-plane compression would naturally force the Sn adatoms up:

the new fact is that the change from down to up is quantized.

Let us, first of all, look at the experimental situation to see whether this picture is compatible with the data. Reports of 2U distortions [76] and actual STM pictures of 2U patches [79] have been indeed reported. That can now be interpreted as due to surface regions with local compressive strain. Another experimental fact is that the distortion, as signaled, e.g., by core level splitting (see chapter 4), is always large, but 3×3 long-range order can be very fragile, with critical temperatures that have been claimed to be as low as 105 K, and/or strongly defect-controlled [79].

While this is hard to explain in a CDW or band Jahn-Teller picture, it is natural in a picture like ours where the main energetics is controlled by a strong on-site double well, and relatively weak inter-site interactions, which naturally yields an order-disorder picture. The difficulty of obtaining clear bands and band dispersions in photoemission must also be related to the intrinsic propensity to disorder.

The heart of our result is that each Sn adatom can be either U or D, but not in between. Moreover we know from previous chapters that very little charge transfer, if any, takes place between U and D adatoms in the 1U cell. Hence it appears that U and D directly reflect two different states of chemical bonding of the adatom to the surface: in short, two different valencies. It is well known in chemistry that Sn and Pb possess two valence states, 4 and 2, the latter being caused by their relatively large s-p splitting. Perhaps the D and U states of Sn can be considered as an attempt of realizing these two valencies. We are currently considering analyzing Mulliken charge populations, and ELF distributions to shed more light on that.

The predominantly kinetic energy gain upon 1U distortion must also be interpreted. When an adatom goes from 0U to 1U, the main electronic effect (Figure 3.3) is a sinking by about 0.2 eV of its combined dangling bond-substrate bond state, a sinking driven by the dangling bond becoming more s-like and less p-like. The kinetic energy decrease can thus be seen as that pertaining to this $p \to s$ partial conversion.

The mixed valence picture of Sn/Ge(111), which we have arrived at, can have rather far-reaching implications. If the 1U and 2U ordered 3×3 states correspond to static mixed valence, one is obviously led to search for corresponding dynamic mixed valence, either thermal, or quantum-mechanical. The high temperature $\sqrt{3} \times \sqrt{3}R30°$ state is to be identified with a thermal dynamical mixed valence. External strain could be used to produce quantum-mechanical mixed valencies: this would happen when in close proximity to any of the classical transitions (0U-1U, 1U-2U, or 2U-3U). At these critical strains, the energy differences between U and D of one or more adatoms get to be so small that quantum tunneling can take over at sufficiently low

temperature. The possibility that such a state could be realized is truly fascinating, and we aim at pursuing it further in the near future.

The apparent 2U signature of the Sn $4d$ core level in the nominally undistorted $\sqrt{3} \times \sqrt{3}R30°$ Sn/Si(111) [77] seems in this context a signature of dynamical mixed valence: in conjunction with G. Profeta, we shall be pursuing that too.

Chapter 7

The Ge(111) high-temperature phase

It is well known that at room temperature, the clean (111) surface of germanium reconstructs with an adatom-rest atom-based $c(2 \times 8)$ pattern [42, 43]. This surface has been accurately described and characterized. The high-temperature behavior of Ge(111) has also been investigated: an extensive series of LEED measurements was taken by Phaneuf and Webb [80], who found evidence of a first-order phase transition at about 300°C.

Namely, at room temperature they observed the diffraction spots corresponding to the well-known $c(2 \times 8)$ reconstruction; when approaching T_c, the higher-order (fourth- and eighth-order) spots first decrease gradually in intensity, and then disappear completely in a very small temperature range (about 3°C), while at the same time, the half-order spots are split each into two distinct spots at incommensurate positions (Figure 7.1). The distance between these two spots increases with temperature, starting from a finite value of about 0.17 $\overset{\circ}{A}^{-1}$ at T_c (Figure 7.2). These data are indicative of a 2×2-based (adatom-rest atom) reconstruction with antiphase domain walls. STM images show a disordered surface [81], suggesting that domains are subject to thermal fluctuation over very rapid time scales: thus a "slow" technique like STM can only observe a time-averaged image of the surface, while diffraction measurements reveal the instantaneous structure.

Other authors have reported different values for the transition temperature T_c, in the range 250–300°C [82, 83].

Modesti and collaborators [84] found that the high-temperature phase is weakly metallic, the surface conductivity increasing roughly linearly from about 500 K, where it's nearly zero, to 1040 K, where the surface melts (Figure 7.3). (The melting temperature for bulk germanium is 1210 K.)
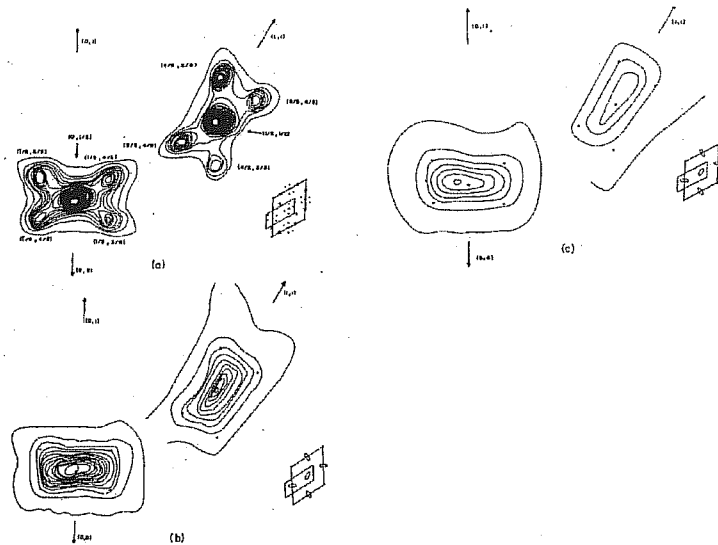
58

Figure 7.1: Intensity contour plot of diffraction spots at (from top to bottom and from left to right): (a) 97°C ($T < T_c$); (b) 297°C ($T \simeq T_c$); (c) 415°C ($T > T_c$) (from Ref. [80]).

7.1 The Phaneuf-Webb model

Phaneuf and Webb [80] proposed a structural model for the Ge(111) high-temperature phase, that we expose here. It is based on the observation that there are four different ways to place a 2 × 2 lattice of adatoms on a (111) substrate, namely, any of the four equivalent T_4 adsorption sites within each 2 × 2 cell can be occupied. Therefore, Phaneuf and Webb proposed that high-temperature Ge(111) is made up of small domains of 2 × 2 phases, each in any of the four possible placements. At the boundary between two adjacent domains, antiphase walls form: such walls are made of a single row of $c(4 \times 2)$ cells. At three-domains boundaries, three concurrent walls forming angles of 120° match, giving rise to a trimer of adatoms, that can be seen as half a $\sqrt{3} \times \sqrt{3}R30°$ unit cell. Each domain must have six walls (some of which however might have zero length) forming angles of 120°: thus the surface appears as a network of irregularly shaped hexagons. The model is illustrated in Figure 7.4.

It is relatively easy for domain walls to move: as shown in Figure 7.5, this is accomplished by the collective motion of a single row of adatoms, each of them being displaced by a 1 × 1 lattice vector (from a T_4 site to another) along the line separating a 2 × 2 domain from a row of $c(4 \times 2)$ cells. By this
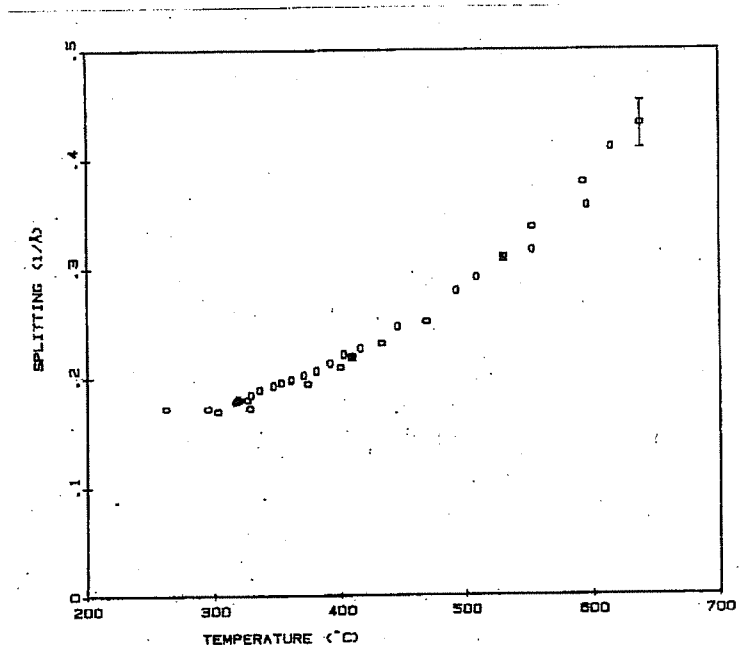
59

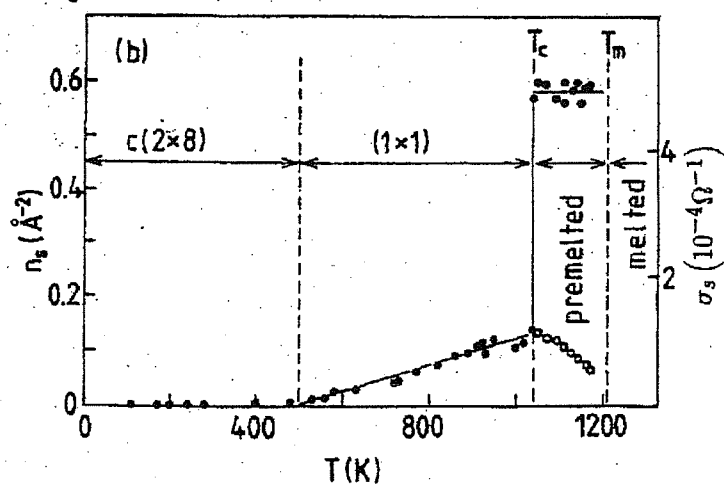Figure 7.2: Splitting of half-order spots as a function of temperature (from Ref. [80]).

Figure 7.3: Surface conductivity as a function of temperature (from Ref. [84]).
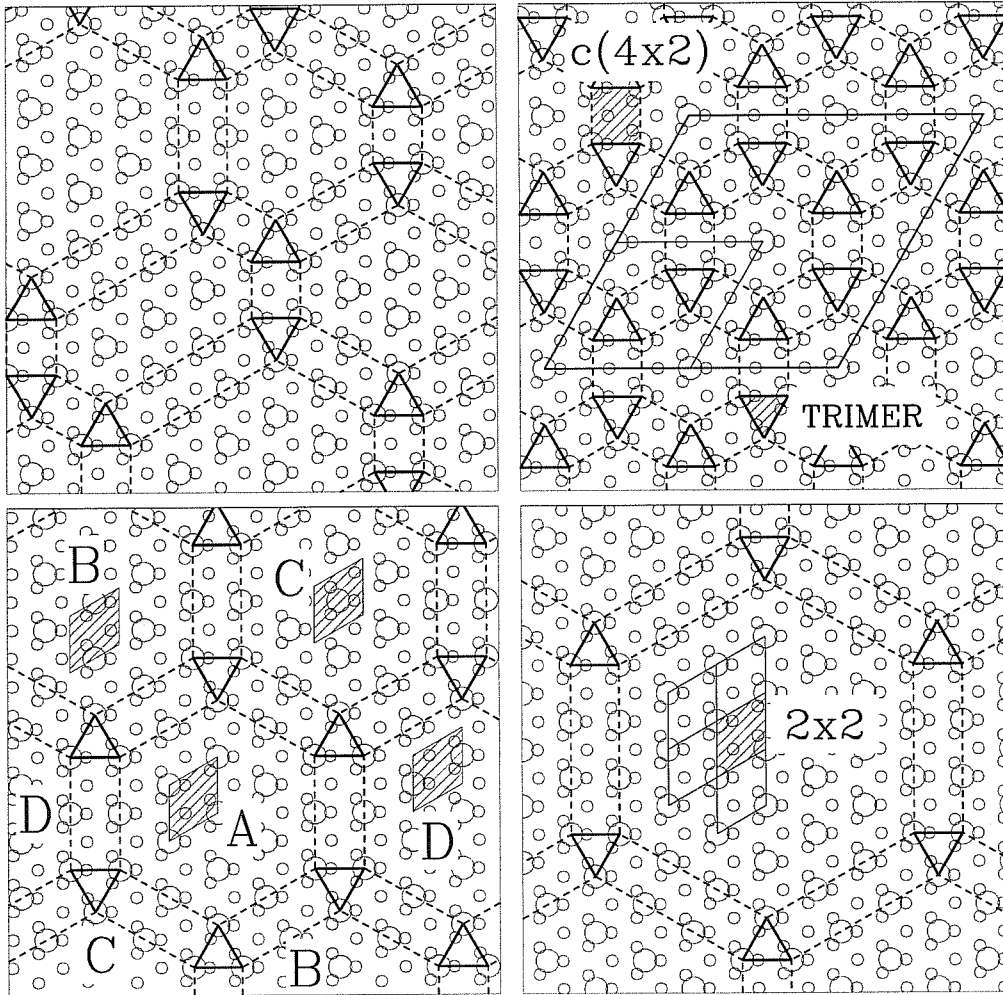
60

Figure 7.4: The Phaneuf-Webb model for the Ge(111) high-temperature phase: (a) an example of an irregularly shaped structure; (b), (c), (d) three regular arrangements of hexagonal domains. In (b) and (d) the 2×2 and $c(4 \times 2)$ building blocks, and the adatom trimers, are shown; in (c) the four possible placements of the 2×2 lattice are shown.
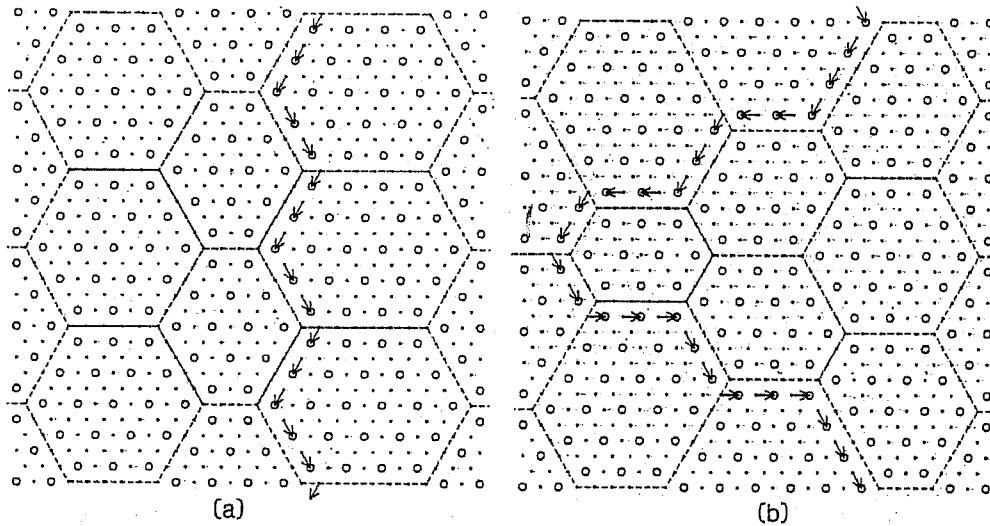
61

Figure 7.5: Domain breathing by the collective motion of a single row of adatoms (from Ref. [80]).

motion, a $c(4 \times 2)$ wall is displaced by a 2×2 lattice vector: as a consequence, one of two adjacent domains is enlarged by a row of 2×2 cells, while the other one is reduced correspondingly. This phenomenon is called "breathing".

Fast breathing of domains can explain why the Phaneuf-Webb structure fails to be observed on the clean Ge(111) surface: actually, a disordered surface is seen by STM images [81], with adatoms randomly placed on the 1×1 lattice of adsorption sites. However, when a small amount ($\ll 1$ ML) of Ga or In is adsorbed on the surface, the extraneous adatoms can "freeze", or at least slow down, the fluctuations, stabilizing domains over time scales sufficiently long to be observed by STM: this has indeed been reported by some authors [85, 86].

7.2 Surface doping by fractional defects

The walls separating adjacent 2×2 domains in the Phaneuf-Webb model are clearly topological. Since there are four possible placements of the 2×2 lattice (labelled A, B, C, D in Figure 7.4(c)), the number of different walls is $\binom{4}{2} = 6$. They are neutral topological defects, having the same density of adatoms (1/4 ML) as the internal of domains; however, at the intersection of any three walls, a trimer of adatoms forms. The latter can be seen as half a $\sqrt{3} \times \sqrt{3}R30°$ cell, with a coverage of 1/3 ML: there is therefore exactly

62

one half extra adatom per trimer. Actually, single trimers can't form (unless we have infinite domains): in a regular arrangement such as that of Figure 7.4(b), there are always exactly two trimers per unit cell. This corresponds to the fact that the hexagonal lattice has a two-point basis. There is thus one extra adatom per unit cell beyond 1/4 ML of coverage; since there's no rest atom paired to this extra adatom, its dangling bond remains half-filled, contributing one extra electron per unit cell, or *one half* extra electron per trimer.

This means that the trimers are zero-dimensional defects, but of a rather unusual kind, because the excess charge associated with the defect is fractional. As a consequence, the excess electron can't be localized on a single defect, but must be shared between two "partner" defects, no matter how far from each other.

To study the behavior of this system, we considered the three regular arrangements shown in Figure 7.4(b), (c), and (d). These are composed by unit cells made of $N + 1$ adatoms and $4N + 3$ atoms per layer, with $N = 6$, 18, and 36; we used 6 Ge layers, plus a layer of H atoms to saturate the bottom surface. The total number of atoms is thus 196, 544, and 1066: since these unit cells are far too large for an *ab initio* treatment, we resorted to the empirical tight-binding scheme [53].

We used the fitting formula by Goodwin *et al.* [87] to compute the tight-binding matrix elements; the empirical coefficients appearing in this formula were fitted so as to reproduce the electron bands obtained from a plane-wave calculation on two smaller cells, namely, the Ge/Ge(111) 2 × 2 and $\sqrt{3} \times \sqrt{3}R30°$ cells considered in chapter 2, truncated to 6 layers of thickness. The precise positions of atoms in the cells were also obtained by taking the optimized positions for the 2 × 2 cell from the same calculation, periodically repeating it, and cutting out hexagonal cells of the required sizes.

The sides of out three cells are $L = 20.8$, 34.7, and 48.6 Å; we assigned a temperature to each cell, by computing the corresponding LEED spots splitting $\delta q = 2\pi/L$, and extracting the dependence of δq on the temperature from the data of Figure 7.2. We obtained $T \simeq 800$ K for the smallest cell, and $T \simeq 600$ K for the medium-sized one, while for the largest cell, δq was smaller than the experimental value just above T_c.

In Figure 7.6 the computed electron bands for the smallest cell ($N = 6$) are shown; the other cells yield a similar picture. There are in each case $N + 1$ surface bands in the middle of the gap: electron counting shows that there is a single electron occupying this bundle of bands, that is, exactly the extra electron per unit cell coming from the two trimer defects. In agreement with experimental evidence, our data show that the system exhibits a weak metallicity. We computed the density of states around the Fermi level, also

0.6

0.4

band energies, eV

0.2

N=6   N=18   N=36

0

E_F

-0.2

0 5 0 5 0 5 10

n(E), 1/eV/ad./spin
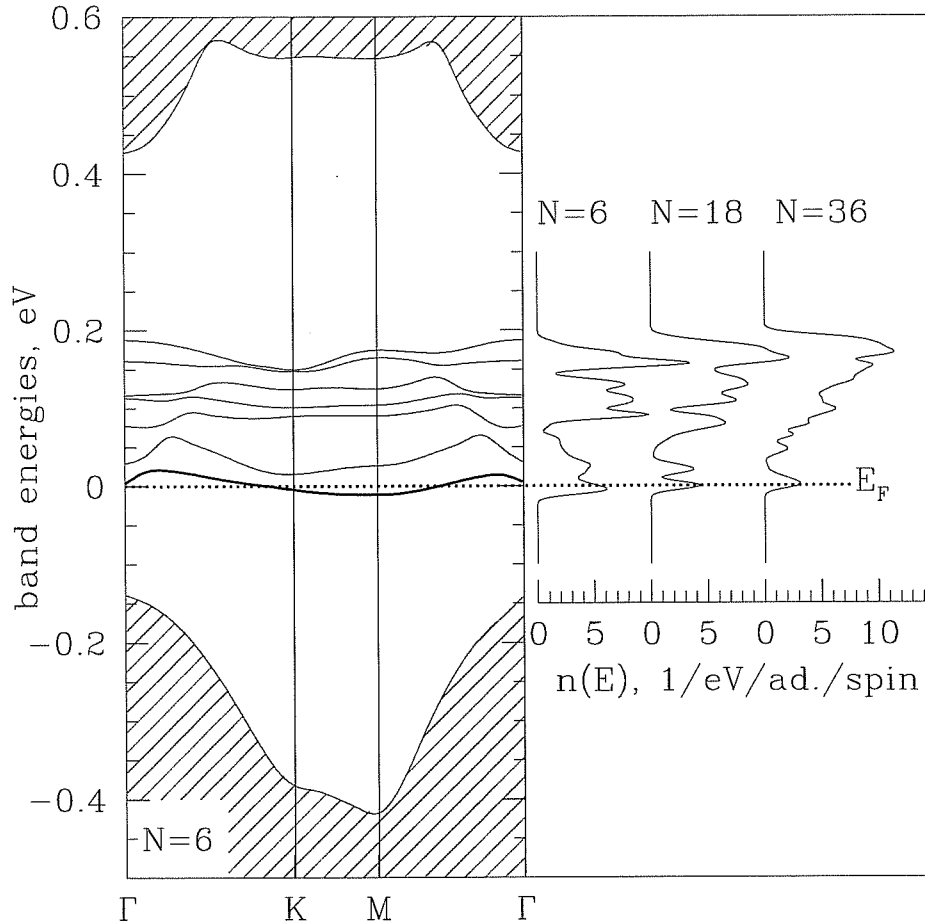
-0.4

N=6

Γ   K   M   Γ

Figure 7.6: (a) Calculated surface bands ($N = 6$); (b) density of states ($N = 6, 18, 36$).

shown in Figure 7.6: $n(E_F)$ is 6.0, 4.3, and 3.0 states/(eV × adatom × spin) for the small, medium, and large cell, respectively.

A plot of the electron density for the half-filled surface state is shown in Figure 7.7. As we see, while the extra electron occupying this state "comes" from adatom trimers at the corners of the hexagon, the state isn't concentrated on trimers only, but also on the domain walls. This reflects the impossibility for the electron to localize on a single trimer: it must continuously "jump" between partner trimers, thus spending a considerable fraction of time on the walls between them. This clearly supports the charge fractionalization picture.

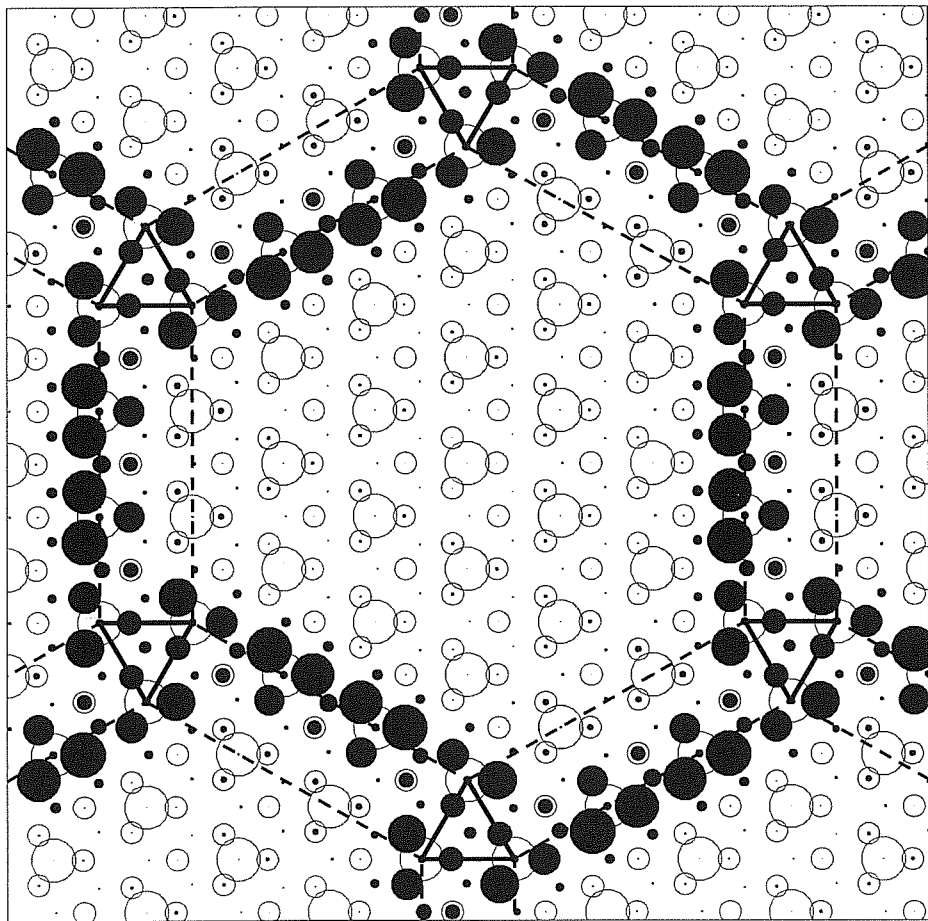We compared our theoretical results with experimental data obtained by

Figure 7.7: Map of the electron density ($N = 36$) for the half-filled surface band at the K point.
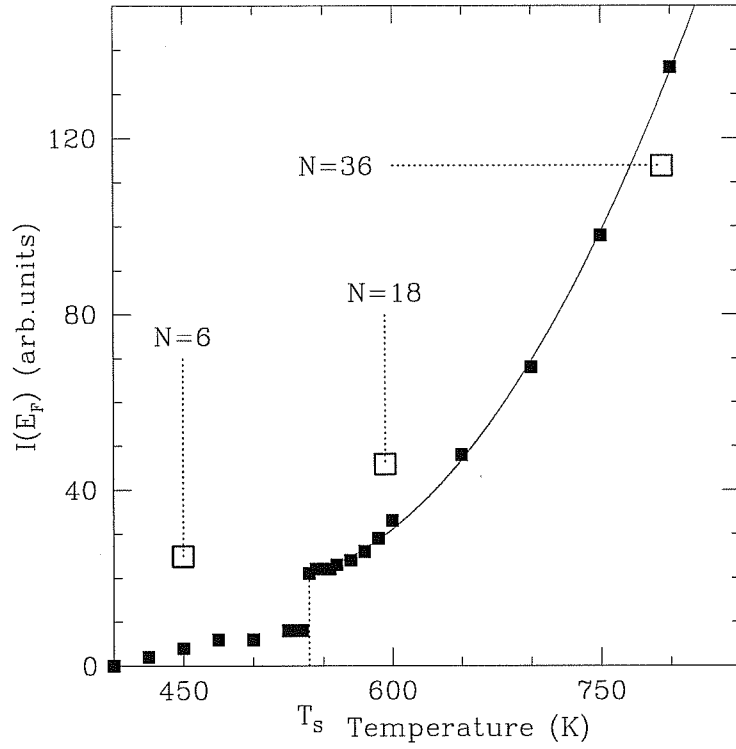
Figure 7.8: Experimental (full circles) and theoretical (open squares) spectral intensity at E_F, as a function of temperature.

A. Goldoni and S. Modesti. A joint report was submitted by us for publication [88]. The results of the comparison are shown in Figure 7.8: the experimental spectral intensity at E_F is plotted, together with theoretical values computed from the electron density of states. The agreement is gratifying.

Conclusions

In this work we have collected a large body of fresh computational evidence on the Sn/Ge(111) surface. While further work is under way to achieve a complete understanding of the physics of this surface, we have already found a number of interesting new facts:

1. We have shown that in the Ge(111) $\sqrt{3} \times \sqrt{3}R30°$ structure (and presumably also on Si(111)), covered by tetravalent adatoms with large atomic number, such as Sn and Pb, the large adatom size forces a downward shift of its dangling bond energy, through a rehybridization mechanism related to the increased angles between the dangling bond and the backbonds. A "coupling" of the dangling bond state with the second-third layer Ge-Ge bond directly beneath adatoms also accounts for enhanced stability.

2. We have calculated that the energy gain in the 3×3 distortion of Sn/Ge(111) comes from electron kinetic energy, while the electron-ion, electron-electron and ion-ion energy terms increase. This points towards a strong intra-adatom dehybridization and to a modulation of the bond with the substrate as the driving mechanism, and is contrary to a charge-density wave (CDW) picture. In CDWs, the sum of electrostatic energies provides the gain, while some kinetic energy is lost: this has also been checked by a model polyacetylene calculation.

3. We have found that the theoretical "up" adatoms core level, on 3×3 Sn/Ge(111), is deeper than that of "down" adatoms: since experiment shows that the deeper component is half as intense as the shallower one, this supports the "1U" pattern of the 3×3 distortion, which is indeed observed by STM. The computed absolute value of the shift also compares fairly well with experiment. This fact also indicates that the difference between inequivalent adatoms is mostly hybridization, but not total charge (that would give the opposite sign to the shift). This is again contrasting with the picture of a CDW.

4. We have also calculated that the work function of Sn/Ge(111) changes very little between the $\sqrt{3} \times \sqrt{3}R30°$ undistorted (unstable) state, and the 3×3, "1 up" distorted state. This indicates a negligible change of surface dipole, which in turn means that the true charge transfer between "up" and "down" adatoms is extremely small. This confirms the conclusions suggested by the core level analysis.

5. We have shown that magnetism plays only a secondary part for the Sn/Ge(111) system. In particular we have ruled out the possibility that a magnetic phase, as is observed in other isoelectronic systems such as Si/Si(111) and Si/SiC(0001), might show good nesting properties and/or exhibit insulating character. A weakly magnetic phase, also presenting a small structural distortion, was actually found by theoretical computations, but it gains little energy over the non-magnetic, undistorted $\sqrt{3} \times \sqrt{3}R30°$ phase, and is at best metastable.

6. We have discovered a completely new aspect of the Sn/Ge(111) surface's behavior by investigating the response of the system under surface strain. We found that strain modifies the *qualitative* pattern of the distortion, namely, it changes from "0U" at large tension (all adatoms down), to "1U" at zero or small strain, to "2U" and finally "3U" (all up) for increasing compression. The "up" and "down" positions are clearly distinct from each other, and change very little with strain. The "up" and "down" states appear as two different "valences" of Sn adatoms, i.e., a "metallic" and a "semiconducting" state, respectively, and thus the Sn/Ge(111) and similar surfaces could be seen as mixed valence systems.

In summary, it appears clear from our data that the explanation of the Sn/Ge(111) 3×3 distortion as a CDW, or more generally as an effect driven by a single, narrow band, must be rejected in favour of a more complex picture involving intraatomic rehybridization, and possibly different valence states of Sn. Further work is under way to obtain a comprehensive interpretation of this phenomenon.

Finally, we have also studied the high-temperature phase (above 540 K) of clean Ge(111). For this phase, we have confirmed the Phaneuf-Webb structural model, and identified a novel fractional charge defect arising from this model. Namely, the Phaneuf-Webb "honeycomb" model is an hexagonal network of zero-dimensional defects of topological nature: the interesting feature of these defects is that they each contribute exactly *half* an electron to the surface bands. There is therefore a continuous motion of electrons between neighboring defects, as a consequence of the impossibility for an

68

electron to localize on a single defect. The resulting fractional doping is also held responsible for the weak metallic behavior seen on this surface by EELS and photoemission.

Acknowledgments

Of course I must thank very much my supervisors, Erio Tosatti, Sandro Scandolo and Stefano de Gironcoli, without whom I wouldn't have been able to do any fruitful research work. Giuseppe Santoro and Gianni Profeta collaborated to this research too. Many thanks come also to the people who wrote the PWSCF program (mainly Stefano de Gironcoli, Stefano Baroni, Paolo Giannozzi and Andrea Del Corso), which has been an essential tool throughout all my work.

I'd like also to thank Erio because, beyond providing constant guidance and physical insight, he has stimulated and helped me to keep on with the fascinating job of physics.

As for the people I've lived with during these years at SISSA, I thank in particular: Stefano Cozzini and Francesco (Franz) Di Tolla for technical help and advice, and also for pleasant discussions; Ugo Tartaglino, for having shared a couple of hotel rooms, many lunchs, and a few bycicle rides; Carlo Cavazzoni, also for technical help, and for our collaboration on FPMD, our discussions on Linux, and our evening pizzas; my office mates throughout these four years, who have welcomed me every morning as I came invariably later than they; and all the people in the SISSA soccer team, in particular Marco Chiaberge and Stefano Piana, for many pleasant evenings together.

Bibliography

[1] P. Hohenberg and W. Kohn. Inhomogeneous electron gas. *Physical Review, 2nd series*, 136(3B):864–871, November 1964.

[2] N. David Mermin. Thermal properties of the inhomogeneous electron gas. *Physical Review, 2nd series*, 137(5A):1441–1443, March 1965.

[3] W. Kohn and L.J. Sham. Self-consistent equations including exchange and correlation effects. *Physical Review, 2nd series*, 140(4A):1133–1138, November 1965.

[4] U. von Barth and L. Hedin. A local exchange-correlation potential for the spin polarized case: I. *Journal of Physics C: solid state physics*, 5:1629–1642, 1972.

[5] D.M. Ceperley and B.J. Alder. Ground state of the electron gas by a stochastic method. *Physical Review Letters*, 45(7):566–569, August 1980.

[6] John P. Perdew and Alex Zunger. Self-interaction correction to density-functional approximations for many-electron systems. *Physical Review B*, 23(10):5048–5079, May 1981.

[7] John P. Perdew and Yue Wang. Accurate and simple analytic representation of the electron-gas correlation energy. *Physical Review B*, 45(23):13244–13249, June 1992.

[8] C.G. Broyden. A class of methods for solving nonlinear simultaneous equations. *Mathematics of Computation*, 19:577–593, 1965.

[9] D.D. Johnson. Modified Broyden's method for accelerating convergence in self-consistent calculations. *Physical Review B*, 38(18):12807–12813, December 1988.

[10] Ernest R. Davidson. Super-matrix methods. *Computer Physics Communications*, 53:49–60, 1989.

[11] Richard Phillips Feynman. Forces in molecules. *Physical Review, 2nd series*, 56:340–343, August 1939.

[12] John P. Perdew, Kieron Burke, and Matthias Ernzerhof. Generalized gradient approximation made simple. *Physical Review Letters*, 77(18):3865–3868, October 1996.

[13] James C. Phillips. Energy-band intrepolation scheme based on a pseudopotential. *Physical Review, 2nd series*, 112(3):685–695, November 1958.

[14] James C. Phillips and Leonard Kleinman. New method for calculating wave functions in crystals and molecules. *Physical Review, 2nd series*, 116(2):287–294, October 1959.

[15] Alex Zunger and Marvin L. Cohen. First-principles nonlocal-pseudopotential approach in the density-functional formalism: development and application to atoms. *Physical Review B*, 18(10):5449–5472, November 1978.

[16] D.R. Hamann, M. Schlüter, and C. Chiang. Norm-conserving pseudopotentials. *Physical Review Letters*, 43(20):1494–1497, November 1979.

[17] G.B. Bachelet, D.R. Hamann, and M. Schlüter. Pseudopotentials that work: from H to Pu. *Physical Review B*, 26(8):4199–4228, October 1982. Erratum: 29(4):2309, February 1984.

[18] N. Troullier and José Luís Martins. Efficient pseudopotentials for plane-wave calculations. *Physical Review B*, 43(3):1993–2006, January 1991.

[19] Leonard Kleinman and D.M. Bylander. Efficacious form for model pseudopotentials. *Physical Review Letters*, 48(20):1425–1428, May 1982.

[20] Milton Abramowitz and Irene A. Stegun, editors. *Handbook of mathematical functions*. Dover Publications, inc., New York, 9th edition, 1970.

[21] Mitchel Weissbluth. *Atoms and molecules*. Academic Press, New York, student edition, 1978.

[22] David Vanderbilt. Optimally smooth norm-conserving pseudopotentials. *Physical Review B*, 32(12):8412–8415, December 1985.

[23] J. Ihm, Alex Zunger, and Marvin L. Cohen. Momentum-space formalism for the total energy of solids. *Journal of Physics C: solid state physics*, 12:4409–4422, 1979.

[24] William H. Press, Brian P. Flannery, Saul A. Teukolsky, and William T. Vettering. *Numerical Recipes. The art of scientific computing.* Cambridge University Press, Cambridge, 1986.

[25] William H. Press, Brian P. Flannery, Saul A. Teukolsky, and William T. Vettering. *Numerical Recipes in C. The art of scientific computing.* Cambridge University Press, Cambridge, 1988.

[26] Neil W. Ashcroft and N. David Mermin. *Solid state physics.* Saunders College, Philadelphia, 1976.

[27] A. Baldereschi. Mean-value point in the Brillouin zone. *Physical Review B*, 7(12):5212–5215, June 1973.

[28] D.J. Chadi and Marvin L. Cohen. Special points in the Brillouin zone. *Physical Review B*, 8(12):5747–5753, December 1973.

[29] Hendrik J. Monkhorst and James D. Pack. Special points for Brillouin-zone integration. *Physical Review B*, 13(12):5188–5192, June 1976.

[30] James D. Pack and Hendrik J. Monkhorst. "Special points for Brillouin-zone integrations"—a reply. *Physical Review B*, 16(4):1748–1749, August 1977.

[31] S.L. Cunningham. Special points in the two-dimensional Brillouin zone. *Physical Review B*, 10(12):4988–4994, December 1974.

[32] Richard J. Needs, Richard M. Martin, and O.H. Nielsen. Total-energy calculations of the structural properties of the group-V element arsenic. *Physical Review B*, 33(6):3778–3784, March 1986.

[33] P. Gomes Da Costa, O.H. Nielsen, and K. Kunc. Stress theorem in the determination of static equilibrium by the density functional method. *Journal of Physics C: solid state physics*, 19:3163–3172, 1986.

[34] Jan Skov Pedersen, Robert Feidenhans'l, Mourits Nielsen, and Kristian Kjær. Adsorbate registry and subsurface relaxation of the α-Ge(111)$\sqrt{3}\times\sqrt{3}$-Sn/Pb reconstructions. *Surface Science*, 189/190:1047–1054, 1987.

[35] M. Göthelid, M. Hammar, C. Törnevik, U.O. Karlsson, N.G. Nilsson, and S.A. Flodström. Sn-induced surface reconstructions on the Ge(111) surface studied with scanning tunneling microscopy. *Surface Science Letters*, 271:357–361, 1992.

[36] J.M. Roesler, M.T. Sieger, T. Miller, and T.C. Chiang. Photoelectron holography of Pb/Si(111)-($\sqrt{3} \times \sqrt{3}$) R30°-β. *Surface Science Letters*, 329:588–592, 1995.

[37] John E. Northrup. Si(111)$\sqrt{3} \times \sqrt{3}$-Al: an adatom-induced reconstruction. *Physical Review Letters*, 53(7):683–686, August 1984.

[38] John E. Northrup. Origin of surface states on Si(111)(7 × 7). *Physical Review Letters*, 57(1):154–157, July 1986.

[39] John E. Northrup and J. Neugebauer. Theory of the adatom-induced reconstruction of the SiC(0001) $\sqrt{3} \times \sqrt{3}$ surface. *Physical Review B*, 52(24):17001–17004, December 1995.

[40] Kunio Takayanagi, Yasumasa Tanishiro, Shigeki Takahashi, and Masaetsu Takahashi. Structure analysis of Si(111)-7×7 reconstructed surface by transmission electron diffraction. *Surface Science*, 164:367–392, 1985.

[41] R.J. Hamers, R.M. Tromp, and J.E. Demuth. Surface electronic structure of Si(111)-(7 × 7) resolved in real space. *Physical Review Letters*, 56(18):1972–1975, May 1986.

[42] D.J. Chadi and C. Chiang. New c-2 × 8 unit cell for the Ge(111) surface. *Physical Review B*, 23(4):1843–1846, February 1981.

[43] R.S. Becker, J.A. Golovchenko, and B.S. Swartzentruber. Tunneling images of germanium surface reconstructions and phase boundaries. *Physical Review Letters*, 54(25):2678–2680, June 1985.

[44] Zhong-Yi Lu. *First-principles study of α-Sn surfaces*. PhD thesis, SISSA/ISAS Scuola Internazionale Superiore di Studi Avanzati/ International School for Advanced Studies, Trieste, October 1996.

[45] J.A. Carlisle, T.Miller, and T.-C. Chiang. Photoemission study of the growth, desorption, Schottky-barrier formation, and atomic structure of Pb on Si(111). *Physical Review B*, 45(7):3400–3409, February 1992.

[46] J.A. Carlisle, T.Miller, and T.-C. Chiang. Photoemission study of Pb on Ge(111). *Physical Review B*, 47(7), February 1993.

[47] Toshihiro Ichikawa and Shozo Ino. Structural study of Sn-induced super-structures on Ge(111) surfaces by RHEED. *Surface Science*, 105:395–428, 1981.

[48] H. Sakurai, K. Higashiyama, S. Kono, and T. Sagawa. X-ray photo-electron diffraction study of the atomic geometry of the Ge(111)($\sqrt{3} \times \sqrt{3}$)R30^0-Sn surface. *Surface Science Letters*, 134:550–556, 1983.

[49] M. Göthelid, T.M. Grehk, M. Hammar, U.O. Karlsson, and S.A. Flod-ström. Adsorption of tin on the Ge(111)-c(2×8) surface studied with scanning tunneling microscopy and photoelectron spectroscopy. *Surface Science*, 328:80–94, 1995.

[50] Gerardo Ballabio, Sandro Scandolo, and Erio Tosatti. $\sqrt{3} \times \sqrt{3}R30°$ versus adatom–rest-atom phases on (111) semiconductor surfaces. *Physical Review B*, 61(20):13345–13348, May 2000.

[51] A.D. Becke. Density-functional exchange-energy approximation with correct asymptotic behavior. *Physical Review A*, 38(6):3098–3100, September 1988.

[52] John P. Perdew. Density-functional approximation for the correlation energy of the inhomogeneous electron gas. *Physical Review B*, 33(12):8822–8824, June 1986. Erratum: 34(10):7406, November 1986.

[53] Walter Ashley Harrison. *Electronic structure and the properties of solids. The physics of the chemical bond.* Dover Publications, inc., New York, 1980.

[54] Stefano de Gironcoli, Sandro Scandolo, Gerardo Ballabio, Giuseppe Santoro, and Erio Tosatti. The mechanism for the 3 × 3 distortion of Sn/Ge(111). *Surface Science*, 454–456:172–177, 2000.

[55] Joseph M. Carpinelli, Hanno H. Weitering, E. Ward Plummer, and Roland Stumpf. Direct observation of a surface charge density wave. *Nature*, 381:398–400, May 1996.

[56] Joseph M. Carpinelli, Hanno H. Weitering, M. Bartkowiak, Roland Stumpf, and E. Ward Plummer. Surface charge ordering transition: α phase of Sn/Ge(111). *Physical Review Letters*, 79(15):2859–2862, October 1997.

[57] A.P. Baddorf, V Jahns, Jiandi Zhang, J.M. Carpinelli, and E. Ward Plummer. Periodic lattice distortion accompanying the (3×3) charge-density-wave phase of Sn/Ge(111). *Physical Review B*, 57(8):4579–4583, February 1998.

[58] Jiandi Zhang, Ismail, P.J. Rous, A.P. Baddorf, and E. Ward Plummer. Periodic lattice distortion accompanying the charge-density-wave transition for Sn-Ge(111). *Physical Review B*, 60(4):2860–2863, July 1999.

[59] Oliver Bunk, J.H. Zeysing, G. Falkenberg, R.L. Johnson, M. Nielsen, M.M. Nielsen, and R. Feidenhans'l. Phase transitions in two dimensions: the case of Sn adsorbed on Ge(111) surfaces. *Physical Review Letters*, 83(11):2226–2229, September 1999.

[60] A. Mascaraque, J. Avila, J. Alvarez, M.C. Asensio, S. Ferrer, and E.G. Michel. Nature of the low-temperature 3 × 3 surface phase of Pb/Ge(111). *Physical Review Letters*, 82(12):2524–2527, March 1999.

[61] J. Avila, A. Mascaraque, E.G. Michel, M.C. Asensio, G. Le Lay, J. Ortega, R. Pérez, and F. Flores. Dynamical fluctuations as the origin of a surface phase transition in Sn/Ge(111). *Physical Review Letters*, 82(2):442–445, January 1999.

[62] J. Ortega, R. Pérez, and F. Flores. A theoretical case study: the Sn/Ge(111)-(3 × 3) surface. *Journal of Physics: Condensed Matter*, 12:L21–L27, 2000.

[63] Andrea Goldoni, C. Cepek, and Silvio Modesti. Temperature and momentum dependence of the spectral function of the charge-density wave and of the normal α phase of Pb/Ge(111). *Physical Review B*, 55(7):4109–4112, February 1997.

[64] Andrea Goldoni and Silvio Modesti. Strong correlation effects in the (3× 3) charge density wave phase of Sn/Ge(111). *Physical Review Letters*, 79(17):3266–3269, October 1997.

[65] Sandro Scandolo, F. Ancilotto, Guido L. Chiarotti, Giuseppe Santoro, Stefano Serra, and Erio Tosatti. First principles calculations of charge and spin density waves of $\sqrt{3}$-adsorbates on semiconductors. *Surface Science*, 402–404:808–812, 1998.

[66] Giuseppe Santoro, Sandro Scandolo, and Erio Tosatti. Charge-density waves and surface Mott insulators for adlayer structures on semiconductors: extended Hubbard modeling. *Physical Review B*, 59(3):1891–1901, January 1999.

[67] John P. Perdew. Unified theory of exchange and correlation beyond the local density approximation. In Paul Ziesche and Helmut Eschrig, editors, *Electronic structure of solids '91*, Physical Research, volume 17, page ?? Akademie Verlag GmbH, Berlin, 1991.

[68] Erio Tosatti and P.W. Anderson. Charge and spin-density waves on semiconductor surfaces. *Japanese Journal of Applied Physics, part 2: Letters*, Suppl. 2:381, 1974.

[69] Erio Tosatti. Electronic superstructures on semiconductor surfaces, and layered transition metal compounds. *Festkörperprobleme (Advances in Solid State Physics)*, 15:113, 1975.

[70] G. Le Lay, V.Yu. Aristov, O. Boström, J.M. Layet, M.C. Asensio, J. Avila, Y. Huttel, and A. Cricenti. Surface charge density waves at Sn/Ge(111)? *Applied Surface Science*, 123/124:440–444, 1998.

[71] R.I.G. Uhrberg and T. Balasubramanian. Electronic structure of the $\sqrt{3} \times \sqrt{3}$-α and 3×3 periodicities of Sn/Ge(111). *Physical Review Letters*, 81(10):2108–2111, September 1998.

[72] John Clarke Slater. *Quantum theory of matter*. Robert E. Krieger Publishing, Huntington, New York, 1977.

[73] E. Pehlke and M. Scheffler. Evidence for site-sensitive screening of core holes at the Si and Ge (001) surface. *Physical Review Letters*, 71(14):2338–2341, October 1993.

[74] Silvio Modesti. Private communication.

[75] V.I. Anisimov, A.E. Bedin, M.A. Korotin, Giuseppe Santoro, Sandro Scandolo, and Erio Tosatti. SiC(0001): a surface Mott-Hubbard insulator. *Physical Review B*, 61(3):1752–1755, January 2000.

[76] J. Avila, A. Mascaraque, G. Le Lay, E.G. Michel, M. Göthelid, H. Ascolani, J. Alvarez, S. Ferrer, and M.C. Asensio. Order-disorder transition driven by dynamical effects between the Sn/Ge(111)-(3×3) and $(\sqrt{3} \times \sqrt{3})R30°$ phases. *Physical Review Letters*, submitted. Preprint: cond-mat/0104259.

[77] M. Göthelid, M. Björqvist, T.M. Grehk, G. Le Lay, and U.O. Karlsson. Metal-semiconductor fluctuation in the Sn adatoms in the Si(111)-Sn and Ge(111)-Sn $(\sqrt{3} \times \sqrt{3})R30°$ reconstructions. *Physical Review B*, 52(20):14352–14355, November 1995.

77

[78] Gianni Profeta. Private communication.

[79] A.V. Melechko, J. Braun, Hanno H. Weitering, and E. Ward Plummer. Role of defects in two-dimensional phase transitions: an STM study of the Sn/Ge(111) system. *Physical Review B*, 61(3):2235–2245, January 2000.

[80] R.J. Phaneuf and M.B. Webb. A LEED study of Ge(111): a high-temperature incommensurate structure. *Surface Science*, 164:167–195, 1985.

[81] R.M. Feenstra, A.M. Slavin, G.A. Held, and M.A. Lutz. Surface diffusion and phase transition on the Ge(111) surface studied by scanning tunneling microscopy. *Physical Review Letters*, 66(25):3257–3260, June 1991.

[82] K. Hricovini, G. Le Lay, M. Abraham, and J.E. Bonnet. Phase transitions on the Ge(111) and Si(111) surfaces from core-level studies. *Physical Review B*, 41(2):1258–1261, January 1990.

[83] M. Abraham, G. Le Lay, and J. Hila. Surface phase transitions on clean Ge(111) studied by spectroscopic ellipsometry. *Physical Review B*, 41(14):9828–9835, May 1990.

[84] Silvio Modesti, V.R. Dhanak, M. Sancrotti, A. Santoni, B.N.J. Persson, and Erio Tosatti. High temperature surface metallization of Ge(111) detected by electron energy loss spectroscopy. *Physical Review Letters*, 73(14):1951–1954, October 1994.

[85] P. Molinàs-Mata and J. Zegenhagen. Gallium-induced perturbations of the Ge(111)-c(2 × 8) reconstruction. *Physical Review B*, 47(16):10319–10325, April 1993.

[86] Zheng Gai, Hongbin Yu, and W.S. Yang. Adatom diffusion on Ge(111) and the corresponding activation energy barrier. *Physical Review B*, 53(20):13547–13550, May 1996.

[87] L. Goodwin, A.J. Skinner, and D.G. Pettifor. Generating transferable tight-binding parameters: application to silicon. *Europhysics Letters*, 9(7):701–706, August 1989.

[88] Gerardo Ballabio, Andrea Goldoni, Silvio Modesti, and Erio Tosatti. Fractional surface doping by topological neutral wall intersections on Ge(111). *Physical Review Letters*, in press.